

# The computation aspects of the equivalent-layer technique: review and perspective

Diego Takahashi <sup>1,\*</sup>, André L. A. Reis <sup>2</sup>, Vanderlei C. Oliveira Jr. <sup>1</sup> and Valéria C. F. Barbosa <sup>1</sup>

<sup>1</sup>*Observatório Nacional, Department of Geophysics, Rio de Janeiro, Brasil*

<sup>2</sup>*Universidade do Estado do Rio de Janeiro, Department of Applied Geology, Rio de Janeiro, Brasil*

Correspondence\*: Valéria C.F. Barbosa  
valcris@on.br

## 2 ABSTRACT

3 Equivalent-layer technique is a powerful tool for processing potential-field data in the space  
4 domain. However, the greatest hindrance for using the equivalent-layer technique is its high  
5 computational cost for processing massive data sets. The large amount of computer memory  
6 usage to store the full sensitivity matrix combined with the computational time required for matrix-  
7 vector multiplications and to solve the resulting linear system, are the main drawbacks that made  
8 unfeasible the use of the equivalent-layer technique for a long time. More recently, the advances in  
9 computational power propelled the development of methods to overcome the heavy computational  
10 cost associated with the equivalent-layer technique. We present a comprehensive review of the  
11 computation aspects concerning the equivalent-layer technique addressing how previous works  
12 have been dealt with the computational cost of this technique. Historically, the high computational  
13 cost of the equivalent-layer technique has been overcome by using a variety of strategies such as:  
14 moving data-window scheme, equivalent data concept, wavelet compression, lower-dimensional  
15 subspace, quadtree discretization, reparametrization of the equivalent layer by a piecewise-  
16 polynomial function, iterative scheme without solving a system of linear equations and the  
17 convolutional equivalent layer using the concept of block-Toeplitz Toeplitz-block (BTTB) matrices.  
18 We compute the number of floating-point operations of some of these strategies adopted in the  
19 equivalent layer technique to show their effectiveness in reducing the computational demand.  
20 Numerically, we also address the stability of some of these strategies used in the equivalent  
21 layer technique by comparing with the stability via the classic equivalent-layer technique with  
22 the zeroth-order Tikhonov regularization. We show that even for the most computational efficient  
23 methods, which can save up to  $10^9$  flops, the linear system stability is maintained. Real data  
24 from Carajás Mineral Province, Brazil is also used to validate the results showing a potential field  
25 transformation.

26 **Keywords:** equivalent layer, gravimetry, fast algorithms, computational cost, stability analysis

## 1 INTRODUCTION

27 In accord with potential theory, a continuous potential-field data (gravity and magnetic data) produced by  
28 any source can be exactly reproduced by a continuous and infinite 2D physical-property surface distribution  
29 that is called the equivalent layer. The equivalent layer is a mathematical solution of Laplace's equation in  
30 the source-free region with the observed potential-field data as the Dirichlet boundary condition (Kellogg,  
31 1929). Grounded on well-established potential theory, the equivalent-layer technique has been used by  
32 exploration geophysicists for processing potential-field data since the late 1960s (Dampney, 1969).

33 Although there was always a great demand for gravity and magnetic data processing, the equivalent-  
34 layer technique has not been massively used. This occurs because its high computational cost makes the  
35 equivalent-layer technique computationally inefficient for processing massive data sets. In the classic  
36 equivalent-layer technique, the continuous problem of the equivalent layer involving integrals is approxi-  
37 mated by a discrete form of the equivalent layer. First, a discrete and finite set of equivalent sources (point  
38 masses, prisms, magnetic dipoles, doublets) is arranged in a layer with finite horizontal dimensions and  
39 located below the observation surface. Next, a linear system of equations is set up with a large and full  
40 sensitivity matrix. Then, a regularized linear inverse problem is solved to estimate the physical property of  
41 each equivalent source within the discrete equivalent layer subject to fitting a discrete set of potential-field  
42 observations. Finally, the estimated physical-property distribution within the equivalent layer is used  
43 to accomplish the desired processing of the potential-field data (e.g., interpolation, upward/downward  
44 continuation, reduction to the pole). The latter step is done by multiplying the matrix of Green's functions  
45 associated with the desired transformation by the estimated physical-property distribution.

46 Beginning in the late 1980s, the equivalent-layer techniques computationally efficient have arose. To  
47 our knowledge, the first method towards improving the efficiency was proposed by Leão and Silva (1989)  
48 who used an overlapping moving-window scheme spanning the data set. The strategy adopted in Leão  
49 and Silva (1989) involves solving several smaller, regularized linear inverse problems instead of one large  
50 problem. This strategy uses a small data window and distributes equivalent sources on a small regular  
51 grid at a constant depth located below the data surface. Leão and Silva (1989) ensure that sources window  
52 extends beyond the boundaries of the data window. For each position of the data window, this scheme  
53 consists in computing the processed field at the center of the data window only and the next estimates  
54 of the processed field are obtained by shifting the data window across the entire dataset. Recently, Soler  
55 and Uieda (2021) developed a computational approach to increase the efficiency of the equivalent-layer  
56 technique by combining two strategies. The first one — the block-averaging source locations — reduces  
57 the model parameters and the second strategy — the gradient-boosted algorithm — reduces the size of the  
58 linear system to be solved by fitting the equivalent source model iteratively along overlapping windows.  
59 Notice that the equivalent-layer strategy of using a moving-window scheme either in Leão and Silva (1989)  
60 or in Soler and Uieda (2021) is similar to discrete convolution.

61 In another approach to reduce computational workload of the equivalent-layer technique Mendonça and  
62 Silva (1994) developed an iterative procedure by incorporating one data point at a time and thus selecting a  
63 smaller data set. This strategy adopted by Mendonça and Silva (1994) is known as 'equivalent data concept'.  
64 Li and Oldenburg (2010) transformed the full sensitivity matrix into a sparse one using the compression  
65 of the coefficient matrix via wavelet transforms based on the orthonormal compactly supported wavelets.  
66 For jointly processing the components of gravity-gradient data using the equivalent-source processing,  
67 Barnes and Lumley (2011) applied the quadtree model discretization to generate a sparse linear system  
68 of equations. Davis and Li (2011) adaptively discretized the model (quadtree model discretization) based  
69 on localized anomalies and used wavelet transforms to reduce, reordered the model parameters (Hilbert

70 space-filling curves) and compressed each row of the sensitivity matrix of the reordered parameter set  
71 (wavelet transforms). By using the subspace method, Mendonça (2020) reduced the dimension of the  
72 linear system of equations to be solved in the equivalent-layer technique. The subspace bases span the  
73 parameter-model space and they are constructed by applying the singular value decomposition to the matrix  
74 containing the gridded data. These strategies followed by Li and Oldenburg (2010), Barnes and Lumley  
75 (2011), Davis and Li (2011) and Mendonça (2020) may be grouped into the strategy of compression  
76 approaches to solve large linear system of equations.

77 Following the strategy of reparametrization of the equivalent layer, Oliveira Jr. et al. (2013) reduced the  
78 model parameters by approximating the equivalent-source layer by a piecewise-polynomial function defined  
79 on a set of user-defined small equivalent-source windows. The estimated parameters are the polynomial  
80 coefficients for each window and they are much smaller than the original number of equivalent sources.  
81 Siqueira et al. (2017) developed an iterative solution where the sensitivity matrix is transformed into a  
82 diagonal matrix with constant terms through the use of the 'excess mass criterion' and of the positive  
83 correlation between the observed gravity data and the masses on the equivalent layer. Jirigalatu and Ebbing  
84 (2019) combined the Gauss-fast Fourier transform (FFT) with Landweber's algorithm and proposed a  
85 fast equivalent-layer technique for jointly processing two-components of the gravity-gradient data. The  
86 Landweber's algorithm has some similarities with gradient-descent algorithm. The strategies worked  
87 out by Siqueira et al. (2017) and Jirigalatu and Ebbing (2019) avoid calculating the Hessian matrix and  
88 solving linear system of equations.

89 Recently, Takahashi et al. (2020, 2022), developed fast and effective equivalent-layer techniques for  
90 processing, respectively, gravity and magnetic data by modifying the forward modeling to estimate the  
91 physical-property distribution over the layer through a 2D discrete convolution that can be efficiently  
92 computed via 2D FFT. These methods took advantage of the Block-Toeplitz Toeplitz-block (BTTB)  
93 structure of the sensitivity matrices, allowing them to be calculated by using only their first column. In  
94 practice, the forward modeling uses a single equivalent source, which significantly reduces the required  
95 RAM memory. Takahashi et al. (2020, 2022) employed the strategy of the convolutional equivalent layer  
96 using the concept of BTTB matrices.

97 Here, we present a comprehensive review of diverse strategies to solve the linear system of the equivalent  
98 layer alongside an analysis of the computational cost and stability of these strategies. To do this analysis  
99 we are using the floating-point operations count to evaluate the performance of a chosen set of methods we  
100 believe are the most used and representative. To test the stability, we are using the linear system sensitivity  
101 to noise as a comparison parameter for the fastest of these methods alongside the classical normal equations.  
102 A potential field transformation will also be used to evaluate the quality of the equivalent sources estimation  
103 results using both synthetic and real data from Carajás Mineral Province, Brazil.

## 2 FUNDAMENTALS

104 Let  $\mathbf{d}$  be a  $D \times 1$  vector, whose  $i$ -th element  $d_i$  is the observed potential field at the position  $(x_i, y_i, z_i)$ ,  
 105  $i \in \{1 : D\}$ , of a topocentric Cartesian system with  $x$ ,  $y$  and  $z$  axes pointing to north, east and down,  
 106 respectively. Consider that  $d_i$  can be satisfactorily approximated by a harmonic function

$$f_i = \sum_{j=1}^P g_{ij} p_j, \quad i \in \{1 : D\}, \quad (1)$$

107 where,  $p_j$  represents the scalar physical property of a virtual source (i.e., monopole, dipole, prism) located  
 108 at  $(x_j, y_j, z_j)$ ,  $j \in \{1 : P\}$  and

$$g_{ij} \equiv g(x_i - x_j, y_i - y_j, z_i - z_j), \quad z_i < \min\{z_j\}, \quad \forall i \in \{1 : D\}, \quad (2)$$

109 is a harmonic function, where  $\min\{z_j\}$  denotes the minimum  $z_j$ , or the vertical coordinate of the shallowest  
 110 virtual source. These virtual sources are called *equivalent sources* and they form an *equivalent layer*. In  
 111 matrix notation, the potential field produced by all equivalent sources at all points  $(x_i, y_i, z_i)$ ,  $i \in \{1 : D\}$ ,  
 112 is given by:

$$\mathbf{f} = \mathbf{G}\mathbf{p}, \quad (3)$$

113 where  $\mathbf{p}$  is a  $P \times 1$  vector with  $j$ -th element  $p_j$  representing the scalar physical property of the  $j$ -th  
 114 equivalent source and  $\mathbf{G}$  is a  $D \times P$  matrix with element  $g_{ij}$  given by equation 2.

115 The equivalent-layer technique consists in solving a linear inverse problem to determine a parameter  
 116 vector  $\mathbf{p}$  leading to a predicted data vector  $\mathbf{f}$  (equation 58) *sufficiently close to* the observed data vector  $\mathbf{d}$ ,  
 117 whose  $i$ -th element  $d_i$  is the observed potential field at  $(x_i, y_i, z_i)$ . The notion of *closeness* is intrinsically  
 118 related to the concept of *vector norm* (e.g., Golub and Loan, 2013, p. 68) or *measure of length* (e.g., ?,  
 119 p. 41). Because of that, almost all methods for determining  $\mathbf{p}$  actually estimate a parameter vector  $\tilde{\mathbf{p}}$   
 120 minimizing a length measure of the difference between  $\mathbf{f}$  and  $\mathbf{d}$  (see subsection 2.3). Given an estimate  $\tilde{\mathbf{p}}$ ,  
 121 it is then possible to compute a potential field transformation

$$\mathbf{t} = \mathbf{A}\tilde{\mathbf{p}}, \quad (4)$$

122 where  $\mathbf{t}$  is a  $T \times 1$  vector with  $k$ -th element  $t_k$  representing the transformed potential field at the position  
 123  $(x_k, y_k, z_k)$ ,  $k \in \{1 : T\}$ , and

$$a_{kj} \equiv a(x_k - x_j, y_k - y_j, z_k - z_j), \quad z_k < \min\{z_j\}, \quad \forall k \in \{1 : T\}, \quad (5)$$

124 is a harmonic function representing the  $kj$ -th element of the  $T \times P$  matrix  $\mathbf{A}$ .

### 125 2.1 Spatial distribution and total number of equivalent sources

126 There is no well-established criteria to define the optimum number  $P$  or the spatial distribution of the  
 127 equivalent sources. We know that setting an equivalent layer with more (less) sources than potential-field  
 128 data usually leads to an underdetermined (overdetermined) inverse problem (e.g., ?, p. 52–53). Concerning  
 129 the spatial distribution of the equivalent sources, the only condition is that they must rely on a surface that  
 130 is located below and does not cross that containing the potential field data. Soler and Uieda (2021) present  
 131 a practical discussion about this topic.

132 From a theoretical point of view, the equivalent layer reproducing a given potential field data set cannot  
 133 cross the true gravity or magnetic sources. This condition is a consequence of recognizing that the equivalent  
 134 layer is essentially an indirect solution of a boundary value problem of potential theory (e.g., ??Dampney,  
 135 1969; ?; ?). In practical applications, however, there is no guarantee that this condition is satisfied. Actually,  
 136 its is widely known from practical experience (e.g., ?) that the equivalent-layer technique works even for  
 137 the case in which the layer cross the true sources.

138 Regarding the depth of the equivalent layer, Dampney (1969) proposed a criterion based on horizontal data  
 139 sampling, suggesting that the equivalent-layer depth should be between two and six times the horizontal  
 140 grid spacing, considering evenly spaced data. However, when dealing with a survey pattern that has  
 141 unevenly spaced data, ? adopted an alternative empirical criterion. According to their proposal, the depth  
 142 of the equivalent layer should range from two to three times the spacing between adjacent flight lines. The  
 143 criteria of Dampney (1969) and ? are valid for planar equivalent layers. Cordell (1992) have proposed  
 144 and an alternative criterion for scattered data that leads to an undulating equivalent layer. This criterion  
 145 have been slightly modified by ?, Guspí and Novara (2009) and Soler and Uieda (2021), for example,  
 146 and consists in setting one equivalent source below each datum at a depth proportional to the horizontal  
 147 distance to the nearest neighboring data points. Soler and Uieda (2021) have compared different strategies  
 148 for defining the equivalent sources depth for the specific problem of interpolating gravity data, but they  
 149 have not found significant differences between them.

## 150 2.2 Matrix G

151 Generally, the harmonic function  $g_{ij}$  (equation 2) is defined in terms of the inverse distance between the  
 152 observation point  $(x_i, y_i, z_i)$  and the  $j$ -th equivalent source at  $(x_j, y_j, z_j)$ ,

$$\frac{1}{r_{ij}} \equiv \frac{1}{\sqrt{(x_i - x_j)^2 + (y_i - y_j)^2 + (z_i - z_j)^2}}, \quad (6)$$

153 or by its partial derivatives of first and second orders, respectively given by

$$\partial_\alpha \frac{1}{r_{ij}} \equiv \frac{-(\alpha_i - \alpha_j)}{r_{ij}^3}, \quad \alpha \in \{x, y, z\}, \quad (7)$$

154 and

$$\partial_{\alpha\beta} \frac{1}{r_{ij}} \equiv \begin{cases} \frac{3(\alpha_i - \alpha_j)^2}{r_{ij}^5}, & \alpha = \beta, \\ \frac{3(\alpha_i - \alpha_j)(\beta_i - \beta_j)}{r_{ij}^5} - \frac{1}{r_{ij}^3}, & \alpha \neq \beta, \end{cases} \quad \alpha, \beta \in \{x, y, z\}. \quad (8)$$

155 In this case, the equivalent layer is formed by punctual sources representing monopoles or dipoles (e.g.,  
 156 Dampney, 1969; ?; Leão and Silva, 1989; Cordell, 1992; Oliveira Jr. et al., 2013; Siqueira et al., 2017; ?;  
 157 ?; Soler and Uieda, 2021; ?). Another common approach consists in not defining  $g_{ij}$  by using equations  
 158 6–8, but other harmonic functions obtained by integrating them over the volume of regular prisms (e.g.,  
 159 ???Jirigalatu and Ebbing, 2019). There are also some less common approaches defining the harmonic  
 160 function  $g_{ij}$  (equation 2) as the potential field due to plane faces with constant physical property (?),  
 161 doublets (?) or by computing the double integration of the inverse distance function with respect to  $z$   
 162 (Guspí and Novara, 2009).

163 A common assumption for most of the equivalent-layer methods is that the harmonic function  $g_{ij}$   
 164 (equation 2) is independent on the actual physical relationship between the observed potential field and

their true sources (e.g., Cordell, 1992; Guspi and Novara, 2009; ?). Hence,  $g_{ij}$  can be defined according to the problem. The only condition imposed to this function is that it decays to zero as the observation point  $(x_i, y_i, z_i)$  goes away from the position  $(x_j, y_j, z_j)$  of the  $j$ -th equivalent source. However, several methods use a function  $g_{ij}$  that preserves the physical relationship between the observed potential field and their true sources. For the case in which the observed potential field is gravity data,  $g_{ij}$  is commonly defined as a component of the gravitational field produced at  $(x_i, y_i, z_i)$  by a point mass or prism located at  $(x_j, y_j, z_j)$ , with unit density. On the other hand,  $g_{ij}$  is commonly defined as a component of the magnetic induction field produced at  $(x_i, y_i, z_i)$  by a dipole or prism located at  $(x_j, y_j, z_j)$ , with unit magnetization intensity, when the observed potential field is magnetic data.

The main challenge in the equivalent-layer technique is the computational complexity associated with handling large datasets. This complexity arises because the sensitivity matrix  $\mathbf{G}$  (equation 58) is dense regardless of the harmonic function  $g_{ij}$  (equation 2) employed. In the case of scattered potential-field data, the structure of  $\mathbf{G}$  is not well-defined, regardless of the spatial distribution of the equivalent sources. However, in a specific scenario where (i) each potential-field datum is directly associated with a single equivalent source located directly below it, and (ii) both the data and sources are based on planar and regularly spaced grids, ?? demonstrate that  $\mathbf{G}$  exhibits a block-Toeplitz Toeplitz-block (BTTB) structure. In such cases, the product of  $\mathbf{G}$  and an arbitrary vector can be efficiently computed using a 2D fast Fourier transform as a discrete convolution.

### 2.3 General formulation

A general formulation for almost all equivalent-layer methods can be achieved by first considering that the  $P \times 1$  parameter vector  $\mathbf{p}$  (equation 58) can be reparameterized into a  $Q \times 1$  vector  $\mathbf{q}$  according to:

$$\mathbf{p} = \mathbf{H} \mathbf{q}, \quad (9)$$

where  $\mathbf{H}$  is a  $P \times Q$  matrix. The predicted data vector  $\mathbf{f}$  (equation 58) can then be rewritten as follows:

$$\mathbf{f} = \mathbf{G} \mathbf{H} \mathbf{q}. \quad (10)$$

Note that the original parameter vector  $\mathbf{p}$  is defined in a  $P$ -dimensional space whereas the reparameterized parameter vector  $\mathbf{q}$  (equation 9) lies in a  $Q$ -dimensional space. For convenience, we use the terms  $P$ -space and  $Q$ -space to designate them.

In this case, the problem of estimating a parameter vector  $\tilde{\mathbf{p}}$  minimizing a length measure of the difference between  $\mathbf{f}$  (equation 58) and  $\mathbf{d}$  is replaced by that of estimating an auxiliary vector  $\tilde{\mathbf{q}}$  minimizing the goal function

$$\Gamma(\mathbf{q}) = \Phi(\mathbf{q}) + \mu \Theta(\mathbf{q}), \quad (11)$$

which is a combination of particular measures of length given by

$$\Phi(\mathbf{q}) = (\mathbf{d} - \mathbf{f})^\top \mathbf{W}_d (\mathbf{d} - \mathbf{f}), \quad (12)$$

and

$$\Theta(\mathbf{q}) = (\mathbf{q} - \bar{\mathbf{q}})^\top \mathbf{W}_q (\mathbf{q} - \bar{\mathbf{q}}), \quad (13)$$

where the regularization parameter  $\mu$  is a positive scalar controlling the trade-off between the data-misfit function  $\Phi(\mathbf{q})$  and the regularization function  $\Theta(\mathbf{q})$ ;  $\mathbf{W}_d$  is a  $D \times D$  symmetric matrix defining the relative

197 importance of each observed datum  $d_i$ ;  $\mathbf{W}_q$  is a  $Q \times Q$  symmetric matrix imposing prior information on  $\mathbf{q}$ ;  
 198 and  $\bar{\mathbf{q}}$  is a  $Q \times 1$  vector of reference values for  $\mathbf{q}$  that satisfies

$$\bar{\mathbf{p}} = \mathbf{H} \bar{\mathbf{q}}, \quad (14)$$

199 where  $\bar{\mathbf{p}}$  is a  $P \times 1$  vector containing reference values for the original parameter vector  $\mathbf{p}$ .

200 After obtaining an estimate  $\tilde{\mathbf{q}}$  for the reparameterized parameter vector  $\mathbf{q}$  (equation 9), the estimate  $\tilde{\mathbf{p}}$  for  
 201 the original parameter vector (equation 58) is computed by

$$\tilde{\mathbf{p}} = \mathbf{H} \tilde{\mathbf{q}}. \quad (15)$$

202 The reparameterized vector  $\tilde{\mathbf{q}}$  is obtained by first computing the gradient of  $\Gamma(\mathbf{q})$ ,

$$\nabla \Gamma(\mathbf{q}) = -2 \mathbf{H}^\top \mathbf{G}^\top \mathbf{W}_d (\mathbf{d} - \mathbf{f}) + 2\mu \mathbf{W}_q (\mathbf{q} - \bar{\mathbf{q}}). \quad (16)$$

203 Then, by considering that  $\nabla \Gamma(\tilde{\mathbf{q}}) = \mathbf{0}$  (equation 16), where  $\mathbf{0}$  is a vector of zeros, as well as adding and  
 204 subtracting the term  $(\mathbf{H}^\top \mathbf{G}^\top \mathbf{W}_d \mathbf{G} \mathbf{H}) \bar{\mathbf{q}}$ , we obtain

$$\tilde{\boldsymbol{\delta}}_q = \mathbf{B} \boldsymbol{\delta}_d, \quad (17)$$

205 where

$$\tilde{\boldsymbol{\delta}}_q = \tilde{\mathbf{q}} - \bar{\mathbf{q}}, \quad (18)$$

$$\boldsymbol{\delta}_d = \mathbf{d} - \mathbf{G} \mathbf{H} \bar{\mathbf{q}}, \quad (19)$$

$$\mathbf{B} = \left( \mathbf{H}^\top \mathbf{G}^\top \mathbf{W}_d \mathbf{G} \mathbf{H} + \mu \mathbf{W}_q \right)^{-1} \mathbf{H}^\top \mathbf{G}^\top \mathbf{W}_d, \quad (20)$$

208 or, equivalently (? , p. 62),

$$\mathbf{B} = \mathbf{W}_q^{-1} \mathbf{H}^\top \mathbf{G}^\top \left( \mathbf{G} \mathbf{H} \mathbf{W}_q^{-1} \mathbf{H}^\top \mathbf{G}^\top + \mu \mathbf{W}_d^{-1} \right)^{-1}. \quad (21)$$

209 Evidently, we have considered that all inverses exist in equations 20 and 21.

210 The  $Q \times D$  matrix  $\mathbf{B}$  defined by equation 20 is commonly used for the case in which  $D > Q$ , i.e., when  
 211 there are more data than parameters (overdetermined problems). In this case, we consider that the estimate  
 212  $\tilde{\mathbf{q}}$  is obtained by solving the following linear system for  $\tilde{\boldsymbol{\delta}}_q$  (equation 18):

$$\left( \mathbf{H}^\top \mathbf{G}^\top \mathbf{W}_d \mathbf{G} \mathbf{H} + \mu \mathbf{W}_q \right) \tilde{\boldsymbol{\delta}}_q = \mathbf{H}^\top \mathbf{G}^\top \mathbf{W}_d \boldsymbol{\delta}_d. \quad (22)$$

213 On the other hand, for the cases in which  $D < Q$  (underdetermined problems), matrix  $\mathbf{B}$  is usually defined  
 214 according to equation 21. In this case, the general approach involves estimating  $\tilde{\mathbf{q}}$  in two steps. The first  
 215 consists in solving a linear system for a dummy vector, which is subsequently used to compute  $\tilde{\mathbf{q}}$  by a  
 216 matrix-vector product as follows:

$$\begin{aligned} \left( \mathbf{G} \mathbf{H} \mathbf{W}_q^{-1} \mathbf{H}^\top \mathbf{G}^\top + \mu \mathbf{W}_d^{-1} \right) \mathbf{u} &= \boldsymbol{\delta}_d \\ \tilde{\boldsymbol{\delta}}_q &= \mathbf{W}_q^{-1} \mathbf{H}^\top \mathbf{G}^\top \mathbf{u} \end{aligned}, \quad (23)$$

217 where  $\mathbf{u}$  is a dummy vector. After obtaining  $\tilde{\boldsymbol{\delta}}_q$  (equations 22 and 23), the estimate  $\tilde{\mathbf{q}}$  is computed with  
218 equation 18.

219 2.3.1 Classical approach

220 The classical approach in the equivalent-layer technique consists in using  $\mathbf{H} = \mathbf{I}_P$ , so that  $P = Q$ ,  $\mathbf{p} = \mathbf{q}$   
221 (equation 9),  $\bar{\mathbf{p}} = \bar{\mathbf{q}}$  (equation 14) and  $\tilde{\mathbf{p}} = \tilde{\mathbf{q}}$  (equation 15). In this case, the linear system (equations 22  
222 and 23) is directly solved for

$$\tilde{\boldsymbol{\delta}}_p = \tilde{\mathbf{p}} - \bar{\mathbf{p}}, \quad (24)$$

223 instead of  $\tilde{\boldsymbol{\delta}}_q$  (equation 18).

### 3 NOTATION FOR SUBVECTORS AND SUBMATRICES

224 Here, we use a notation inspired on that presented by (Van Loan, 1992, p. 4) to represent subvectors and  
225 submatrices. Subvectors of  $\mathbf{d}$ , for example, are specified by  $\mathbf{d}[\mathbf{i}]$ , where  $\mathbf{i}$  is a list of integer numbers that  
226 “pick out” the elements of  $\mathbf{d}$  forming the subvector  $\mathbf{d}[\mathbf{i}]$ . For example,  $\mathbf{i} = (1, 6, 4, 6)$  gives the subvector  
227  $\mathbf{d}[\mathbf{i}] = [d_1 \ d_6 \ d_4 \ d_6]^\top$ . Note that the list  $\mathbf{i}$  of indices may be sorted or not and it may also have repeated  
228 indices. For the particular case in which the list has a single element  $\mathbf{i} = (i)$ , then it can be used to extract  
229 the  $i$ -th element  $d_i \equiv \mathbf{d}[i]$  of  $\mathbf{d}$ . Sequential lists with increment of 1, if the starting index is smaller than the  
230 final index, or  $-1$ , if the starting index is greater than the final index, can be represented by using the colon  
231 notation. For example,

$$\begin{aligned}\mathbf{i} = (3 : 8) &\Leftrightarrow \mathbf{d}[\mathbf{i}] = [d_3 \ d_4 \ \dots \ d_8]^\top \\ \mathbf{i} = (8 : 3) &\Leftrightarrow \mathbf{d}[\mathbf{i}] = [d_8 \ d_7 \ \dots \ d_3]^\top \\ \mathbf{i} = (: 8) &\Leftrightarrow \mathbf{d}[\mathbf{i}] = [d_1 \ d_2 \ \dots \ d_8]^\top \\ \mathbf{i} = (3 :) &\Leftrightarrow \mathbf{d}[\mathbf{i}] = [d_3 \ d_4 \ \dots \ d_D]^\top\end{aligned},$$

232 where  $D$  is the number of elements forming  $\mathbf{d}$ .

233 The notation above can also be used to define submatrices of the  $D \times P$  matrix  $\mathbf{G}$ . For example,  
234  $\mathbf{i} = (2, 7, 4, 6)$  and  $\mathbf{j} = (1, 3, 8)$  lead to the submatrix

$$\mathbf{G}[\mathbf{i}, \mathbf{j}] = \begin{bmatrix} g_{21} & g_{23} & g_{28} \\ g_{71} & g_{73} & g_{78} \\ g_{41} & g_{43} & g_{48} \\ g_{61} & g_{63} & g_{68} \end{bmatrix}.$$

235 Note that, in this case, the lists  $\mathbf{i}$  and  $\mathbf{j}$  “pick out”, respectively, the rows and columns of  $\mathbf{G}$  that form the  
236 submatrix  $\mathbf{G}[\mathbf{i}, \mathbf{j}]$ . The  $i$ -th row of  $\mathbf{G}$  is given by the  $1 \times P$  vector  $\mathbf{G}[i, :]$ . Similarly, the  $D \times 1$  vector  $\mathbf{G}[:, j]$   
237 represents the  $j$ -th column. Finally, we may use the colon notation to define the following submatrix:

$$\mathbf{i} = (2 : 5), \mathbf{j} = (3 : 7) \Leftrightarrow \mathbf{G}[\mathbf{i}, \mathbf{j}] = \begin{bmatrix} g_{23} & g_{24} & g_{25} & g_{26} & g_{27} \\ g_{33} & g_{34} & g_{35} & g_{36} & g_{37} \\ g_{43} & g_{44} & g_{45} & g_{46} & g_{47} \\ g_{53} & g_{54} & g_{55} & g_{56} & g_{57} \end{bmatrix},$$

238 which contains the contiguous elements of  $\mathbf{G}$  from rows 2 to 5 and from columns 3 to 7.

## 4 COMPUTATIONAL STRATEGIES

239 Here, we review some strategies for reducing the computational cost of equivalent-layer technique. Typically, estimating a parameter vector  $\tilde{\mathbf{p}}$  or  $\tilde{\mathbf{q}}$  requires to solve a large-scale linear inversion (equations 22 and 23). This, in turn, means to deal with some obstacles concerning large computational cost:

- 242 (i) the large computer memory to store large and full matrices;  
 243 (ii) the long computation time to multiply a matrix by a vector; and  
 244 (iii) the long computation time to solve a large linear system of equations.

245 Two important factors affecting the efficiency of a given matrix algorithm are the storage and amount of required arithmetic. Here, we quantify this last factor by counting *flops*, which are floating point additions, subtractions, multiplications or divisions (Golub and Loan, 2013, p. 12–14). We focus on the overall strategies used by the selected methods.

249 **4.1 Moving window**

250 The initial approach to enhance the computational efficiency of the equivalent-layer technique is commonly denoted *moving window* and involves first splitting the observed data  $d_i$ ,  $i \in \{1 : D\}$ , into  $M$  overlapping subsets (or data windows) formed by  $D^m$  data each,  $m \in \{1 : M\}$ . The data inside the  $m$ -th window are usually adjacent to each other and have indices defined by an integer list  $\mathbf{i}^m$  having  $D^m$  elements. The number of data  $D^m$  forming the data windows are not necessarily equal to each other. 255 Each data window has a  $D^m \times 1$  observed data vector  $\mathbf{d}^m \equiv \mathbf{d}[\mathbf{i}^m]$ . The second step consists in defining 256 a set of  $P$  equivalent sources with scalar physical property  $p_j$ ,  $j \in \{1 : P\}$ , and also split them into  $M$  257 overlapping subsets (or source windows) formed by  $P^m$  data each,  $m \in \{1 : M\}$ . The sources inside the 258  $m$ -th window have indices defined by an integer list  $\mathbf{j}^m$  having  $P^m$  elements. Each source window has a 259  $P^m \times 1$  parameter vector  $\mathbf{p}^m$  and is located right below the corresponding  $m$ -th data window. Then, each 260  $\mathbf{d}^m \equiv \mathbf{d}[\mathbf{i}^m]$  is approximated by

$$\mathbf{f}^m = \mathbf{G}^m \mathbf{p}^m, \quad (25)$$

261 where  $\mathbf{G}^m \equiv \mathbf{G}[\mathbf{i}^m, \mathbf{j}^m]$  is a submatrix of  $\mathbf{G}$  (equation 58) formed by the elements computed with equation 262 2 using only the data and equivalent sources located inside the window  $m$ -th. The main idea of the moving- 263 window approach is using the  $\tilde{\mathbf{p}}^m$  estimated for each window to obtain (i) an estimate  $\tilde{\mathbf{p}}$  of the parameter 264 vector for the entire equivalent layer or (ii) a given potential-field transformation  $\mathbf{t}$  (equation 4). The main 265 advantages of this approach is that (i) the estimated parameter vector  $\tilde{\mathbf{p}}$  or transformed potential field are 266 not obtained by solving the full, but smaller linear systems and (ii) the full matrix  $\mathbf{G}$  (equation 58) is never 267 stored.

268 Leão and Silva (1989) presented a pioneer work using the moving-window approach. Their method 269 requires a regularly-spaced grid of observed data on a horizontal plane  $z_0$ . The data windows are defined by 270 square local grids of  $\sqrt{D'} \times \sqrt{D'}$  adjacent points, all of them having the same number of points  $D'$ . The 271 equivalent sources in the  $m$ -th data window are located below the observation plane, at a constant vertical 272 distance  $\Delta z_0$ . They are arranged on a regular grid of  $\sqrt{P'} \times \sqrt{P'}$  adjacent points following the same 273 grid pattern of the observed data. The local grid of sources for all data windows have the same number 274 of elements  $P'$ . Besides, they are vertically aligned, but expands the limits of their corresponding data 275 windows, so that  $D' < P'$ . Because of this spatial configuration of observed data and equivalent sources, 276 we have that  $\mathbf{G}^m = \mathbf{G}'$  (equation 25) for all data windows (i.e.,  $\forall m \in \{1 : M\}$ ), where  $\mathbf{G}'$  is a  $D' \times P'$  277 constant matrix.

278 By omitting the normalization strategy used by Leão and Silva (1989), their method consists in directly  
 279 computing the transformed potential field  $t_c^m$  at the central point  $(x_c^m, y_c^m, z_0 + \Delta z_0)$  of each data window  
 280 as follows:

$$t_c^m = (\mathbf{a}')^\top \mathbf{B}' \mathbf{d}^m, \quad m \in \{1 : M\}, \quad (26)$$

281 where  $\mathbf{a}'$  is a  $P' \times 1$  vector with elements computed by equation 5 by using all equivalent sources in the  
 282  $m$ -th window and only the coordinate of the central point in the  $m$ -th data window and

$$\mathbf{B}' = (\mathbf{G}')^\top \left[ \mathbf{G}' (\mathbf{G}')^\top + \mu \mathbf{I}_{D'} \right]^{-1} \quad (27)$$

283 is a particular case of matrix  $\mathbf{B}$  associated with underdetermined problems (equation 21) for the particular  
 284 case in which  $\mathbf{H} = \mathbf{W}_q = \mathbf{I}_{P'}$  (equations 9 and 13),  $\mathbf{W}_d = \mathbf{I}_{D'}$  (equation 12),  $\tilde{\mathbf{p}} = \mathbf{0}$  (equation 14), where  
 285  $\mathbf{I}_{P'}$  and  $\mathbf{I}_{D'}$  are identity matrices of order  $P'$  and  $D'$ , respectively, and  $\mathbf{0}$  is a vector of zeros. Due to the  
 286 presumed spatial configuration of the observed data and equivalent sources,  $\mathbf{a}'$  and  $\mathbf{G}'$  are the same for all  
 287 data windows. Hence, only the data vector  $\mathbf{d}^m$  is modified according to the position of the data window.  
 288 Note that equation 26 combines the potential-field transformation (equation 4) with the solution of the  
 289 undetermined problem (equation 23).

290 The method proposed by Leão and Silva (1989) can be outlined by the Algorithm 1. Note that Leão and  
 291 Silva (1989) directly compute the transformed potential  $t_c^m$  at the central point of each data window without  
 292 explicitly computing and storing an estimated for  $\mathbf{p}^m$  (equation 25). It means that their method allows  
 293 computing a single potential-field transformation. A different transformation or the same one evaluated at  
 294 different points require running their moving-data window method again.

---

**Algorithm 1:** Generic pseudo-code for the method proposed by Leão and Silva (1989).

---

**Initialization :**

- 1 Set the indices  $\mathbf{i}^m$  for each data window,  $m \in \{1 : M\}$  ;
  - 2 Set the indices  $\mathbf{j}^m$  for each source window,  $m \in \{1 : M\}$  ;
  - 3 Set the constant depth  $z_0 + \Delta z_0$  for all equivalent sources ;
  - 4 Compute the vector  $\mathbf{a}'$  associated with the desired potential-field transformation ;
  - 5 Compute the matrix  $\mathbf{G}'$  ;
  - 6 Compute the matrix  $\mathbf{B}'$  (equation 27) ;
  - 7 Compute the vector  $(\mathbf{a}')^\top \mathbf{B}'$  ;
  - 8  $m = 1$  ;
  - 9 **while**  $m < M$  **do**
  - 10   | Compute  $t_c^m$  (equation 26) ;
  - 11   |  $m \leftarrow m + 1$  ;
  - 12 **end**
- 

295 Soler and Uieda (2021) generalized the method proposed by Leão and Silva (1989) for irregularly spaced  
 296 data on an undulating surface. A direct consequence of this generalization is that a different submatrix  
 297  $\mathbf{G}^m \equiv \mathbf{G}[\mathbf{i}^m, \mathbf{j}^m]$  (equation 25) must be computed for each window. Differently from Leão and Silva  
 298 (1989), Soler and Uieda (2021) store the computed  $\tilde{\mathbf{p}}^m$  for all windows and subsequently use them to obtain  
 299 a desired potential-field transformation (equation 4) as the superposed effect of all windows. The estimated  
 300  $\tilde{\mathbf{p}}^m$  for all windows are combined to form a single  $P \times 1$  vector  $\tilde{\mathbf{p}}$ , which is an estimate for original  
 301 parameter vector  $\mathbf{p}$  (equation 58). For each data window, Soler and Uieda (2021) solve an overdetermined  
 302 problem (equation 22) for  $\tilde{\mathbf{p}}^m$  by using  $\mathbf{H} = \mathbf{W}_q = \mathbf{I}_{P^m}$  (equations 9 and 13),  $\mathbf{W}_d^m$  (equation 12) equal to

303 a diagonal matrix of weights for the data inside the  $m$ -th window and  $\bar{\mathbf{p}} = \mathbf{0}$  (equation 14), so that

$$\left[ (\mathbf{G}^m)^\top \mathbf{W}_d^m \mathbf{G}^m + \mu \mathbf{I}_{P'} \right] \tilde{\mathbf{p}}^m = (\mathbf{G}^m)^\top \mathbf{W}_d^m \mathbf{d}^m. \quad (28)$$

304 Unlike Leão and Silva (1989), Soler and Uieda (2021) do not adopt a sequential order of the data  
 305 windows; rather, they adopt a randomized order of windows in their iterations. The overall steps of the  
 306 method proposed by Soler and Uieda (2021) are defined by the Algorithm 2. For convenience, we have  
 307 omitted the details about the randomized window order and the normalization strategy employed by Soler  
 308 and Uieda (2021). Note that this algorithm starts with a residuals vector  $\mathbf{r}$  that is iteratively updated. The  
 309 iterative algorithm in Soler and Uieda (2021) estimates a solution ( $\tilde{\mathbf{p}}^m$  in equation 28) using the data and  
 310 the equivalent sources that fall within a moving-data window; however, it calculates the predicted data  
 311 and the residual data in the whole survey data. Next, the residual data that fall within a new position of  
 312 the data window is used as input data to estimate a new solution within the data window which, in turn, is  
 313 used to calculate a new predicted data and a new residual data in the whole survey data. Regarding the  
 314 equivalent-source layout, Soler and Uieda (2021) proposed the block-averaged sources locations in which  
 315 the survey area is divided into horizontal blocks and one single equivalent source is assigned to each block.  
 316 Each single source per block is placed over the layer with its horizontal coordinates given by the average  
 317 horizontal positions of observation points. According to Soler and Uieda (2021), the block-averaged  
 318 sources layout may prevent aliasing of the interpolated values, specially when the observations are unevenly  
 319 sampled. This strategy also reduces the number of equivalent sources without affecting the accuracy of  
 320 the potential-field interpolation. This reduction reduces the computational load for estimating the physical  
 321 property on the equivalent layer. This block-averaged sources layout is not included in the Algorithm 2.

---

**Algorithm 2:** Generic pseudo-code for the method proposed by Soler and Uieda (2021).
 

---

**Initialization :**

- 1 Set the indices  $i^m$  for each data window,  $m \in \{1 : M\}$  ;
  - 2 Set the indices  $j^m$  for each source window,  $m \in \{1 : M\}$  ;
  - 3 Set the depth of all equivalent sources ;
  - 4 Set a  $D \times 1$  residuals vector  $\mathbf{r} = \mathbf{d}$  ;
  - 5 Set a  $P \times 1$  vector  $\tilde{\mathbf{p}} = \mathbf{0}$  ;
  - 6  $m = 1$  ;
  - 7 **while**  $m < M$  **do**
  - 8   Set the matrix  $\mathbf{W}_d^m$  ;
  - 9   Compute the matrix  $\mathbf{G}^m$  ;
  - 10   Compute  $\tilde{\mathbf{p}}^m$  (equation 28) ;
  - 11    $\tilde{\mathbf{p}}[j^m] \leftarrow \tilde{\mathbf{p}}[j^m] + \tilde{\mathbf{p}}^m$  ;
  - 12    $\mathbf{r} \leftarrow \mathbf{r} - \mathbf{G}[:, j^m] \tilde{\mathbf{p}}^m$  ;
  - 13    $m \leftarrow m + 1$  ;
  - 14 **end**
- 

322 **4.2 Column-action update**

323 We call the computational strategy *column-action update* because a single source is used to calculate the  
 324 predicted data and the residual data in the whole survey data. Hence, a single column of the sensitivity  
 325 matrix  $\mathbf{G}$  (equation 58) is calculated iteratively.

326 Cordell (1992) proposed a computational strategy that was later used by Guspí and Novara (2009) and  
 327 relies on first defining one equivalent source located right below each observed data  $d_i$ ,  $i \in \{1 : D\}$ , at  
 328 a vertical coordinate  $z_i + \Delta z_i$ , where  $\Delta z_i$  is proportional to the distance from the  $i$ -th observation point  
 329 ( $x_i, y_i, z_i$ ) to its closest neighbor. The second step consists in updating the physical property  $p_j$  of a single  
 330 equivalent source,  $j \in \{1 : D\}$  and remove its predicted potential field from the observed data vector  $d$ ,  
 331 producing a residuals vector  $r$ . At each iteration, the single equivalent source is the one located vertically  
 332 beneath the observation station of the maximum data residual. Next, the predicted data produced by this  
 333 single source is calculated over all of the observation points and a new data residual  $r$  and the  $D \times 1$   
 334 parameter vector  $p$  containing the physical property of all equivalent sources are updated iteratively. During  
 335 each subsequent iteration, Cordell's method either incorporates a single equivalent source or adjusts an  
 336 existing equivalent source to match the maximum amplitude of the current residual field. The convergence  
 337 occurs when all of the residuals are bounded by an envelope of prespecified expected error. At the end, the  
 338 algorithm produces an estimate  $\tilde{p}$  for the parameter vector yielding a predicted potential field  $f$  (equation  
 339 58) satisfactorily fitting the observed data  $d$  according to a given criterion. Note that the method proposed  
 340 by Cordell (1992) iteratively solves the linear  $G\tilde{p} \approx d$  with a  $D \times D$  matrix  $G$ . At each iteration, only a  
 341 single column of  $G$  (equation 58) is used. An advantage of this *column-action update approach* is that the  
 342 full matrix  $G$  is never stored.

343 Algorithm 3 delineates the Cordell's method. Note that a single column  $G[:, i_{\max}]$  of the  $D \times D$  matrix  $G$   
 344 (equation 58) is used per iteration, where  $i_{\max}$  is the index of the maximum absolute value in  $r$ . As pointed  
 345 out by Cordell (1992), the method does not necessarily decrease monotonically along the iterations. Besides,  
 346 the method may not converge depending on how the vertical distances  $\Delta z_i$ ,  $i \in \{1 : D\}$ , controlling the  
 347 depths of the equivalent sources are set. According to Cordell (1992), the maximum absolute value  $r_{\max}$   
 348 in  $r$  decreases robustly at the beginning and oscillates within a narrowing envelope for the subsequent  
 349 iterations.

350 Guspí and Novara (2009) generalized Cordell's method to perform reduction to the pole and other  
 351 transformations on scattered magnetic observations by using two steps. The first step involves computing  
 352 the vertical component of the observed field using equivalent sources while preserving the magnetization  
 353 direction. In the second step, the vertical observation direction is maintained, but the magnetization  
 354 direction is shifted to the vertical. The main idea employed by both Cordell (1992) and Guspí and Novara  
 355 (2009) is an iterative scheme that uses a single equivalent source positioned below a measurement station  
 356 to compute both the predicted data and residual data for all stations. This approach entails a computational  
 357 strategy where a single column of the sensitivity matrix  $G$  (equation 58) is calculated per iteration.

### 358 4.3 Row-action update

359 We call the computational strategy *row-action update* because a single row of the sensitivity matrix  $G$   
 360 (equation 58) is calculated iteratively. Hence, the equivalent-layer solution is updated by processing a  
 361 new datum (one matrix row) at each iteration. To reduce the total processing time and memory usage of  
 362 equivalent-layer technique, Mendonça and Silva (1994) proposed a strategy called *equivalent data concept*.  
 363 The equivalent data concept is grounded on the principle that there is a subset of redundant data that does  
 364 not contribute to the final solution and thus can be dispensed. Conversely, there is a subset of observations,  
 365 called equivalent data, that contributes effectively to the final solution and fits the remaining observations  
 366 (redundant data). Iteratively, Mendonça and Silva (1994) selected the subset of equivalent data that is  
 367 substantially smaller than the original dataset. This selection is carried out by incorporating one data point  
 368 at a time.

**Algorithm 3:** Generic pseudo-code for the method proposed by Cordell (1992).**Initialization :**


---

```

1 Compute a  $D \times 1$  vector  $\Delta z$  whose  $i$ -th element  $\Delta z_i$  is a vertical distance controlling the depth of
   the  $i$ -th equivalent source,  $i \in \{1 : D\}$  ;
2 Set a tolerance  $\epsilon$  ;
3 Set a maximum number of iterations ITMAX ;
4 Set a  $D \times 1$  residuals vector  $r = d$  ;
5 Set a  $D \times 1$  vector  $\tilde{p} = 0$  ;
6 Define the maximum absolute value  $r_{\max}$  in  $r$  ;
7  $m = 1$  ;
8 while ( $r_{\max} > \epsilon$ ) and ( $m < \text{ITMAX}$ ) do
9   Define the coordinates  $(x_{\max}, y_{\max}, z_{\max})$  and index  $i_{\max}$  of the observation point associated with
       $r_{\max}$  ;
10   $\tilde{p}[i_{\max}] \leftarrow \tilde{p}[i_{\max}] + (r_{\max} \Delta z[i_{\max}])$  ;
11   $r \leftarrow r - (\mathbf{G}[:, i_{\max}] \tilde{p}[i_{\max}])$  ;
12  Define the new  $r_{\max}$  in  $r$  ;
13   $m \leftarrow m + 1$  ;
14 end

```

---

369 Mendonça and Silva (1994) proposes an algebraic reconstruction technique (ART) (e.g., ?, p. 58) to  
 370 estimate a parameter vector  $\tilde{p}$  for a regular grid of  $P$  equivalent sources on a horizontal plane  $z_0$ . Such  
 371 methods iterate on the linear system rows to estimate corrections for the parameter vector, which may  
 372 substantially save computer time and memory required to compute and store the full linear system matrix  
 373 along the iterations. The convergence of such *row-update methods* depends on the linear system condition.  
 374 The main advantage of such methods is not computing and storing the full linear system matrix, but  
 375 iteratively using its rows. In contrast to ART-type algorithms, the rows in Mendonça and Silva (1994) are  
 376 not processed sequentially. Instead, in Mendonça and Silva (1994), the rows are introduced according to  
 377 their residual magnitudes (maximum absolute value in  $r$ ), which are computed based on the estimate over  
 378 the equivalent layer from the previous iteration. The particular ART method proposed by Mendonça and  
 379 Silva (1994) considers that

$$\mathbf{d} = \begin{bmatrix} \mathbf{d}_e \\ \mathbf{d}_r \end{bmatrix}, \quad \mathbf{G} = \begin{bmatrix} \mathbf{G}_e \\ \mathbf{R}_r \end{bmatrix}, \quad (29)$$

380 where  $\mathbf{d}_e$  and  $\mathbf{d}_r$  are  $D_e \times 1$  and  $D_r \times 1$  vectors and  $\mathbf{G}_e$  and  $\mathbf{G}_r$  are  $D_e \times P$  and  $D_r \times P$  matrices,  
 381 respectively. Mendonça and Silva (1994) designate  $\mathbf{d}_e$  and  $\mathbf{d}_r$  as, respectively, *equivalent* and *redundant*  
 382 data. With the exception of a normalization strategy, Mendonça and Silva (1994) calculate a  $P \times 1$  estimated  
 383 parameter vector  $\tilde{p}$  by solving an underdetermined problem (equation 23) involving only the equivalent  
 384 data  $\mathbf{d}_e$  (equation 29) for the particular case in which  $\mathbf{H} = \mathbf{W}_p = \mathbf{I}_P$  (equations 9 and 13),  $\mathbf{W}_d = \mathbf{I}_{D_e}$   
 385 (equation 12) and  $\bar{p} = 0$  (equation 14), which results in

$$\begin{aligned} (\mathbf{F} + \mu \mathbf{I}_{D_e}) \mathbf{u} &= \mathbf{d}_e \\ \tilde{p} &= \mathbf{G}_e^\top \mathbf{u} \end{aligned}, \quad (30)$$

386 where  $\mathbf{F}$  is a computationally-efficient  $D_e \times D_e$  matrix that approximates  $\mathbf{G}_e \mathbf{G}_e^\top$ . Mendonça and Silva  
 387 (1994) presume that the estimated parameter vector  $\tilde{p}$  obtained from equation 30 leads to a  $D_r \times 1$  residuals  
 388 vector

$$\mathbf{r} = \mathbf{d}_r - \mathbf{G}_r \tilde{p} \quad (31)$$

389 having a maximum absolute value  $r_{\max} \leq \epsilon$ , where  $\epsilon$  is a predefined tolerance.

390 The overall method of Mendonça and Silva (1994) is defined by Algorithm 4. It is important noting  
 391 that the number  $D_e$  of equivalent data in  $\mathbf{d}_e$  increases by one per iteration, which means that the order  
 392 of the linear system in equation 30 also increases by one at each iteration. Those authors also propose a  
 393 computational strategy based on Cholesky factorization (e.g., Golub and Loan, 2013, p. 163) for efficiently  
 394 updating  $(\mathbf{F} + \mu \mathbf{I}_{D_e})$  at a given iteration (line 16 in Algorithm 4) by computing only its new elements with  
 395 respect to those computed in the previous iteration.

---

**Algorithm 4:** Generic pseudo-code for the method proposed by Mendonça and Silva (1994).
 

---

**Initialization :**

```

1 Set a regular grid of  $P$  equivalent sources at a horizontal plane  $z_0$  ;
2 Set a tolerance  $\epsilon$  ;
3 Set a  $D \times 1$  residuals vector  $\mathbf{r} = \mathbf{d}$  ;
4 Define the maximum absolute value  $r_{\max}$  in  $\mathbf{r}$  ;
5 Define the index  $i_{\max}$  of  $r_{\max}$  ;
6 Define the list of indices  $\mathbf{i}_r$  of the remaining data in  $\mathbf{r}$  ;
7 Define  $\mathbf{d}_e = \mathbf{d}[i_{\max}]$  ;
8 Compute  $(\mathbf{F} + \mu \mathbf{I}_{D_e})$  and  $\mathbf{G}_e$  ;
9 Compute  $\tilde{\mathbf{p}}$  (equation 30) ;
10 Compute  $\mathbf{r} = \mathbf{d}[\mathbf{i}_r] - \mathbf{G}[\mathbf{i}_r, :] \tilde{\mathbf{p}}$  ;
11 Define the maximum absolute value  $r_{\max}$  in  $\mathbf{r}$  ;
12 while ( $r_{\max} > \epsilon$ ) do
13   Define the index  $i_{\max}$  of  $r_{\max}$  ;
14   Define the list of indices  $\mathbf{i}_r$  of the remaining elements in  $\mathbf{r}$  ;
15    $\mathbf{d}_e \leftarrow \begin{bmatrix} \mathbf{d}_e \\ \mathbf{d}[i_{\max}] \end{bmatrix}$  ;
16   Update  $(\mathbf{F} + \mu \mathbf{I}_{D_e})$  and  $\mathbf{G}_e$  ;
17   Update  $\tilde{\mathbf{p}}$  (equation 30) ;
18   Update  $\mathbf{r} = \mathbf{d}[\mathbf{i}_r] - \mathbf{G}[\mathbf{i}_r, :] \tilde{\mathbf{p}}$  ;
19   Define the maximum absolute value  $r_{\max}$  in  $\mathbf{r}$  ;
20 end
```

---

396 **4.4 Reparameterization**

397 Another approach for improving the computational performance of equivalent-layer technique consists  
 398 in setting a  $P \times Q$  reparameterization matrix  $\mathbf{H}$  (equation 9) with  $Q \ll P$ . This strategy has been used  
 399 in applied geophysics for decades (e.g., Skilling and Bryan, 1984; Kennett et al., 1988; Oldenburg et al.,  
 400 1993; Barbosa et al., 1997) and is known as *subspace method*. The main idea relies in reducing the linear  
 401 system dimension from the original  $P$ -space to a lower-dimensional subspace (the  $Q$ -space). An estimate  
 402  $\tilde{\mathbf{q}}$  for the reparameterized parameter vector  $\mathbf{q}$  is obtained in the  $Q$ -space and subsequently used to obtain  
 403 an estimate  $\tilde{\mathbf{p}}$  for the parameter vector  $\mathbf{p}$  (equation 58) in the  $P$ -space by using equation 9. Hence, the key  
 404 aspect of this *reparameterization approach* is solving an appreciably smaller linear inverse problem for  $\tilde{\mathbf{q}}$   
 405 than that for the original parameter vector  $\tilde{\mathbf{p}}$  (equation 58).

406 Oliveira Jr. et al. (2013) have used this approach to describe the physical property distribution on the  
 407 equivalent layer in terms of piecewise bivariate polynomials. Specifically, their method consists in splitting  
 408 a regular grid of equivalent sources into source windows inside which the physical-property distribution  
 409 is described by bivariate polynomial functions. The key aspect of their method relies on the fact that the

410 total number of coefficients required to define the bivariate polynomials is considerably smaller than the  
 411 original number of equivalent sources. Hence, they formulate a linear inverse problem for estimating the  
 412 polynomial coefficients and use them later to compute the physical property distribution on the equivalent  
 413 layer.

414 The method proposed by Oliveira Jr. et al. (2013) consists in solving an overdetermined problem (equation  
 415 22) for estimating the polynomial coefficients  $\tilde{\mathbf{q}}$  with  $\mathbf{W}_d = \mathbf{I}_D$  (equation 12) and  $\bar{q} = 0$  (equation 14), so  
 416 that

$$(H^\top G^\top G H + \mu W_q) \tilde{\mathbf{q}} = H^\top G^\top \mathbf{d}, \quad (32)$$

417 where  $W_q = H^\top W_p H$  is defined by a matrix  $W_p$  representing the zeroth- and first-order Tikhonov  
 418 regularization (e.g., ?, p. 103). Note that, in this case, the prior information is defined in the  $P$ -space for the  
 419 original parameter vector  $\mathbf{p}$  and then transformed to the  $Q$ -space. Another characteristic of their method is  
 420 that it is valid for processing irregularly-spaced data on an undulating surface.

421 ? also proposed a reparameterization approach for the equivalent-layer technique. Their approach,  
 422 however, consists in setting  $H$  as a truncated singular value decomposition (SVD) (e.g., ?, p. 55) of the  
 423 observed potential field. Differently from Oliveira Jr. et al. (2013), however, the method of ? requires  
 424 a regular grid of potential-field data on horizontal plane. Another difference is that these authors uses  
 425  $W_q = I_Q$  (equation 13), which means that the regularization is defined directly in the  $Q$ -space.

426 Before Oliveira Jr. et al. (2013) and ?, ? also proposed a computationally efficient method for equivalent-  
 427 layer technique based on reparameterization. A key difference, however, is that ? did not set a  $P \times Q$   
 428 reparameterization matrix  $H$  (equation 9) with  $Q \ll P$ . Instead, they used a matrix  $H$  with  $Q \approx 1.7P$ .  
 429 Their central idea is setting a reparameterization scheme that groups distant equivalent sources into blocks  
 430 by using a bisection process. This scheme leads to a quadtree representation of the physical-property  
 431 distribution on the equivalent layer, so that matrix  $GH$  (equation 10) is notably sparse. ? explore this  
 432 sparsity in solving the overdetermined problem for  $\tilde{\mathbf{q}}$  (equation 32) via conjugate-gradient method (e.g.,  
 433 Golub and Loan, 2013, sec. 11.3).

#### 434 4.5 Wavelet compression

435 Previously to ?, the idea of transforming the dense matrix  $G$  (equation 58) into a sparse one has already  
 436 been used in the context of equivalent-layer technique. ? proposed a method that applies the discrete  
 437 wavelet transform to introduce sparsity into the original dense matrix  $G$ . Those authors approximate a  
 438 planar grid of potential-field data by a regularly-spaced grid of equivalent sources, so that the number of  
 439 data  $D$  and sources  $P$  is the same, i.e.,  $D = P$ . Specifically, ? proposed a method that applies the wavelet  
 440 transform to the original dense matrix  $G$  and sets to zero the small coefficients that are below a given  
 441 threshold, which results in an approximating sparse representation of  $G$  in the wavelet domain. They first  
 442 consider the following approximation

$$\mathbf{d}_w \approx \mathbf{G}_s \mathbf{p}_w, \quad (33)$$

443 where

$$\mathbf{d}_w = \mathcal{W} \mathbf{d}, \quad \mathbf{p}_w = \mathcal{W} \mathbf{p}, \quad (34)$$

444 are the observed data and parameter vector in the wavelet domain;  $\mathcal{W}$  is a  $D \times D$  orthogonal matrix  
 445 defining a discrete wavelet transform; and  $\mathbf{G}_s$  is a sparse matrix obtained by setting to zero the elements of

$$\mathbf{G}_w = \mathcal{W} \mathbf{G} \mathcal{W}^\top \quad (35)$$

446 with absolute value smaller than a given threshold.

447 ? solve a normalized inverse problem in the wavelet domain. Specifically, they first define a matrix

$$\mathbf{G}_L = \mathbf{G}_s \mathbf{L}^{-1} \quad (36)$$

448 and a normalized parameter vector

$$\mathbf{p}_L = \mathbf{L} \mathbf{p}_w , \quad (37)$$

449 where  $\mathbf{L}$  is a diagonal and invertible matrix representing an approximation of the first-order Tikhonov  
450 regularization in the wavelet domain. Then they solve an overdetermined problem (equation 22) to obtain  
451 an estimate  $\tilde{\mathbf{p}}_L$  for  $\mathbf{p}_L$  (equation 37), with  $\mathbf{G}_L$  (equation 36),  $\mathbf{H} = \mathbf{I}_P$  (equations 9),  $\mu = 0$  (equation 11),  
452  $\mathbf{W}_d = \mathbf{I}_D$  (equation 12) and  $\bar{p} = 0$  (equation 14) via conjugate-gradient method (e.g., Golub and Loan,  
453 2013, sec. 11.3). Finally, ? compute an estimate  $\tilde{\mathbf{p}}$  for the original parameter vector given by

$$\tilde{\mathbf{p}} = \mathcal{W}^\top (\mathbf{L}^{-1} \tilde{\mathbf{p}}_L) , \quad (38)$$

454 where the term within parenthesis is an estimate  $\tilde{\mathbf{p}}_w$  of the parameter vector  $\mathbf{p}_w$  (equation 34) in the wavelet  
455 domain and matrix  $\mathcal{W}^\top$  represents an inverse wavelet transform.

## 456 4.6 Iterative methods using the full matrix G

457 Xia and Sprowl (1991) introduced an iterative method for estimating the parameter vector  $\tilde{\mathbf{p}}$  (equation  
458 58), which was subsequently adapted to the Fourier domain by Xia et al. (1993). Their method uses the full  
459 and dense sensitivity matrix  $\mathbf{G}$  (equation 58) (without applying any compression or reparameterization, for  
460 example) to compute the predicted data at all observation points per iteration. More than two decades later,  
461 Siqueira et al. (2017) have proposed an iterative method similar to that presented by Xia and Sprowl (1991).  
462 The difference is that Siqueira et al.'s algorithm was deduced from the *Gauss' theorem* (e.g., ?, p. 43) and  
463 the *total excess of mass* (e.g., ?, p. 60). Besides, Siqueira et al. (2017) have included a numerical analysis  
464 showing that their method produces very stable solutions, even for noise-corrupted potential-field data.

465 The iterative method proposed by Siqueira et al. (2017) is outlined in Algorithm 5, presumes an equivalent  
466 layer formed by monopoles (point masses) and can be applied to irregularly-spaced data on an undulating  
467 surface. Note that the residuals  $\mathbf{r}$  are used to compute a correction  $\Delta\mathbf{p}$  for the parameter vector at each  
468 iteration (line 11), which requires a matrix-vector product involving the full matrix  $\mathbf{G}$ . Interestingly, this  
469 approach for estimating the physical property distribution on an equivalent layer is the same originally  
470 proposed by ? for estimating the basement relief under sedimentary basins. The methods of Xia and  
471 Sprowl (1991) and Siqueira et al. (2017) were originally proposed for processing gravity data, but can  
472 be potentially applied to any harmonic function because they actually represent iterative solutions of the  
473 classical *Dirichlet's problem* or the *first boundary value problem of potential theory* (? , p. 236) on a plane.

474 Recently, Jirigalatu and Ebbing (2019) presented another iterative method for estimating a parameter  
475 vector  $\tilde{\mathbf{p}}$  (equation 58). With the purpose of combining different potential-field data, their method basically  
476 modifies that shown in Algorithm 5 by changing the initial approximation and the iterative correction for  
477 the parameter vector. Specifically, Jirigalatu and Ebbing (2019) replace line 4 by  $\tilde{\mathbf{p}} = \mathbf{0}$ , where  $\mathbf{0}$  is a vector  
478 of zeros, and line 9 by  $\Delta\mathbf{p} = \omega \mathbf{G}^\top \mathbf{r}$ , where  $\omega$  is a positive scalar defined by trial and error. Note that  
479 this modified approach requires two matrix-vector products involving the full matrix  $\mathbf{G}$  per iteration. To  
480 overcome the high computational cost of these two products, Jirigalatu and Ebbing (2019) set an equivalent

481 layer formed by prisms and compute their predicted potential field in the wavenumber domain by using the  
 482 Gauss-FFT technique ?.

---

**Algorithm 5:** Generic pseudo-code for the iterative method proposed by Siqueira et al. (2017). The symbol “ $\circ$ ” denotes the entrywise or Hadamard product (e.g., ?, p. 298) and  $\sigma$  is a  $P \times 1$  vector whose  $j$ -th element is the ratio of a predefined element of area centered at the  $j$ -th equivalent source and the term  $2\pi\gamma$ , where  $\gamma$  is the gravitational constant.

---

**Initialization :**

```

1 Set  $P$  equivalent sources on a horizontal plane  $z_0$  ;
2 Set a tolerance  $\epsilon$  ;
3 Set an auxiliary vector  $\sigma$  ;
4 Compute  $\tilde{\mathbf{p}} = \sigma \circ \mathbf{d}$  ;
5 Compute  $\mathbf{G}$  (equation 58) ;
6 Compute  $\mathbf{r} = \mathbf{d} - \mathbf{G} \tilde{\mathbf{p}}$  ;
7 Compute  $\delta = \|\mathbf{r}\|/D$  ;
8 while ( $\delta > \epsilon$ ) do
9   | Compute  $\Delta\mathbf{p} = \sigma \circ \mathbf{r}$  ;
10  | Update  $\tilde{\mathbf{p}} \leftarrow \tilde{\mathbf{p}} + \Delta\mathbf{p}$  ;
11  | Compute  $\nu = \mathbf{G} \Delta\mathbf{p}$  ;
12  | Update  $\mathbf{r} \leftarrow \mathbf{r} - \nu$  ;
13  | Compute  $\delta = \|\nu\|/D$  ;
14 end
```

---

483 **4.7 Discrete convolution**

484 Recently, ?? proposed the *convolutional equivalent-layer method*, which explores the structure of the  
 485 sensitivity matrix  $\mathbf{G}$  (equation 58) for the particular case in which (i) there is a single equivalent source  
 486 right below each potential-field datum and (ii) both data and sources rely on planar and regularly spaced  
 487 grids. Specifically, they consider a regular grid of  $D$  potential-field data at points  $(x_i, y_i, z_0)$ ,  $i \in \{1 : D\}$ ,  
 488 on a horizontal plane  $z_0$ . The data indices  $i$  may be ordered along the  $x$ - or  $y$ -direction, which results  
 489 in an  $x$ - or  $y$ -oriented grid, respectively. They also consider a single equivalent source located right  
 490 below each datum, at a constant vertical coordinate  $z_0 + \Delta z$ ,  $\Delta z > 0$ . In this case, the number of data  
 491 and equivalent sources are equal to each other (i.e.,  $D = P$ ) and  $\mathbf{G}$  (equation 58) assumes a *doubly block*  
 492 *Toeplitz* (? , p. 28) or *block-Toeplitz Toeplitz-block* (BTTB) (? , p. 67) structure formed by  $D_B \times D_B$  blocks,  
 493 where each block has  $D_b \times D_b$  elements, with  $D = D_B D_b$ . This particular structure allows formulating  
 494 the product of  $\mathbf{G}$  and an arbitrary vector as a *fast 2D discrete convolution* via *Fast Fourier Transform* (FFT)  
 495 (Van Loan, 1992, section 4.2).

496 Consider, for example, the particular case in which  $D_B = 4$ ,  $D_b = 3$  and  $D = 12$ . In this case,  $\mathbf{G}$   
 497 (equation 58) is a  $12 \times 12$  block matrix given by

$$\mathbf{G} = \begin{bmatrix} \mathbf{G}^0 & \mathbf{G}^1 & \mathbf{G}^2 & \mathbf{G}^3 \\ \mathbf{G}^{-1} & \mathbf{G}^0 & \mathbf{G}^1 & \mathbf{G}^2 \\ \mathbf{G}^{-2} & \mathbf{G}^{-1} & \mathbf{G}^0 & \mathbf{G}^1 \\ \mathbf{G}^{-3} & \mathbf{G}^{-2} & \mathbf{G}^{-1} & \mathbf{G}^0 \end{bmatrix}_{D \times D}, \quad (39)$$

498 where each block  $\mathbf{G}^\ell$ ,  $\ell \in \{(1 - D_B) : (D_B - 1)\}$ , is a  $3 \times 3$  Toeplitz matrix. ?? have deduced the specific  
 499 relationship between blocks  $\mathbf{G}^\ell$  and  $\mathbf{G}^{-\ell}$  and also between a given block  $\mathbf{G}^\ell$  and its transposed  $(\mathbf{G}^\ell)^\top$

according to the harmonic function  $g_{ij}$  (equation 2) defining the element  $ij$  of the sensitivity matrix  $\mathbf{G}$  (equation 58) and the orientation of the data grid.

Consider the matrix-vector products

$$\mathbf{G} \mathbf{v} = \mathbf{w} \quad (40)$$

and

$$\mathbf{G}^\top \mathbf{v} = \mathbf{w}, \quad (41)$$

involving a  $D \times D$  sensitivity matrix  $\mathbf{G}$  (equation 58) defined in terms of a given harmonic function  $g_{ij}$  (equation 2), where

$$\mathbf{v} = \begin{bmatrix} \mathbf{v}^0 \\ \vdots \\ \mathbf{v}^{D_B-1} \end{bmatrix}_{D \times 1}, \quad \mathbf{w} = \begin{bmatrix} \mathbf{w}^0 \\ \vdots \\ \mathbf{w}^{D_B-1} \end{bmatrix}_{D \times 1}, \quad (42)$$

are arbitrary partitioned vectors formed by  $D_B$  sub-vectors  $\mathbf{v}^\ell$  and  $\mathbf{w}^\ell$ ,  $\ell \in \{0 : (D_B - 1)\}$ , all of them having  $D_b$  elements. Equations 40 and 41 can be computed in terms of an auxiliary matrix-vector product

$$\mathbf{G}_c \mathbf{v}_c = \mathbf{w}_c, \quad (43)$$

where

$$\mathbf{v}_c = \begin{bmatrix} \mathbf{v}_c^0 \\ \vdots \\ \mathbf{v}_c^{D_B-1} \\ \mathbf{0}_{2D \times 1} \end{bmatrix}_{4D \times 1}, \quad \mathbf{w}_c = \begin{bmatrix} \mathbf{w}_c^0 \\ \vdots \\ \mathbf{w}_c^{D_B-1} \\ \mathbf{0}_{2D \times 1} \end{bmatrix}_{4D \times 1}, \quad (44)$$

are partitioned vectors formed by  $2D_b \times 1$  sub-vectors

$$\mathbf{v}_c^\ell = \begin{bmatrix} \mathbf{v}^\ell \\ \mathbf{0}_{D_b \times 1} \end{bmatrix}_{2D_b \times 1}, \quad \mathbf{w}_c^\ell = \begin{bmatrix} \mathbf{w}^\ell \\ \mathbf{0}_{D_b \times 1} \end{bmatrix}_{2D_b \times 1}, \quad (45)$$

and  $\mathbf{G}_c$  is a  $4D \times 4D$  *doubly block circulant* (? , p. 28) or *block-circulant circulant-block* (BCCB) (? , p. 76) matrix. What follows aims at explaining how the original matrix-vector products defined by equations 40 and 41, involving a  $D \times D$  BTTB matrix  $\mathbf{G}$  exemplified by equation 39, can be efficiently computed in terms of the auxiliary matrix-vector product given by equation 43, which has a  $4D \times 4D$  BCCB matrix  $\mathbf{G}_c$ .

Matrix  $\mathbf{G}_c$  (equation 43) is formed by  $2D_B \times 2D_B$  blocks, where each block  $\mathbf{G}_c^\ell$ ,  $\ell \in \{(1 - D_B) : (D_B - 1)\}$  is a  $2D_b \times 2D_b$  circulant matrix. For the case in which the original matrix-vector product is that defined by equation 40, the first column of blocks forming the BCCB matrix  $\mathbf{G}_c$  is given by

$$\mathbf{G}_c[:, : 2D_b] = \begin{bmatrix} \mathbf{G}_c^0 \\ \mathbf{G}_c^{-1} \\ \vdots \\ \mathbf{G}_c^{1-D_B} \\ \mathbf{0}_{2D_b \times 2D_b} \\ \mathbf{G}_c^{D_B-1} \\ \vdots \\ \mathbf{G}_c^1 \end{bmatrix}_{4D \times 2D_b}, \quad (46)$$

517 with blocks  $\mathbf{G}_c^\ell$  having the first column given by

$$\mathbf{G}_c^\ell[:, 1] = \begin{bmatrix} \mathbf{G}^\ell[:, 1] \\ 0 \\ (\mathbf{G}^\ell[1, D_b : 2])^\top \end{bmatrix}_{2D_b \times 2D_b}, \quad \ell \in \{(1 - D_B) : (D_B - 1)\}, \quad (47)$$

518 where  $\mathbf{G}^\ell$  are the blocks forming the BTTB matrix  $\mathbf{G}$  (equation 39). For the case in which the original  
519 matrix-vector product is that defined by equation 41, the first column of blocks forming the BCCB matrix  
520  $\mathbf{G}_c$  is given by

$$\mathbf{G}_c[:, : 2D_b] = \begin{bmatrix} \mathbf{G}_c^0 \\ \mathbf{G}_c^1 \\ \vdots \\ \mathbf{G}_c^{D_B-1} \\ \mathbf{0}_{2D_b \times 2D_b} \\ \mathbf{G}_c^{1-D_B} \\ \vdots \\ \mathbf{G}_c^{-1} \end{bmatrix}_{4D \times 2D_b}, \quad (48)$$

521 with blocks  $\mathbf{G}_c^\ell$  having the first column given by

$$\mathbf{G}_c^\ell[:, 1] = \begin{bmatrix} (\mathbf{G}^\ell[1, :])^\top \\ 0 \\ \mathbf{G}^\ell[D_b : 2, 1] \end{bmatrix}_{2D_b \times 2D_b}, \quad \ell \in \{(1 - D_B) : (D_B - 1)\}. \quad (49)$$

522 The complete matrix  $\mathbf{G}_c$  (equation 43) is obtained by properly downshifting the block columns  $\mathbf{G}_c[:, : 2D_b]$  defined by equations 46 or 48. Similarly, the  $\ell$ -th block  $\mathbf{G}_c^\ell$  of  $\mathbf{G}_c$  is obtained by properly downshifting  
523 the first columns  $\mathbf{G}_c^\ell[:, 1]$  defined by equations 47 or 49.

525 Note that  $\mathbf{G}_c$  (equation 43) is a  $4D \times 4D$  matrix and  $\mathbf{G}$  (equation 39) is a  $D \times D$  matrix. It seems weird  
526 to say that computing  $\mathbf{G}_c \mathbf{v}_c$  is more efficient than directly computing  $\mathbf{G} \mathbf{v}$ . To understand this, we need first  
527 to use the fact that BCCB matrices are diagonalized by the 2D unitary discrete Fourier transform (DFT)  
528 (e.g., Davis, 1979, p. 31). Because of that,  $\mathbf{G}_c$  can be written as

$$\mathbf{G}_c = (\mathcal{F}_{2D_B} \otimes \mathcal{F}_{2D_b})^* \Lambda (\mathcal{F}_{2D_B} \otimes \mathcal{F}_{2D_b}), \quad (50)$$

529 where the symbol “ $\otimes$ ” denotes the Kronecker product (e.g., ?, p. 243),  $\mathcal{F}_{2D_B}$  and  $\mathcal{F}_{2D_b}$  are the  $2D_B \times 2D_B$   
530 and  $2D_b \times 2D_b$  unitary DFT matrices (e.g., Davis, 1979, p. 31), respectively, the superscript “ $*$ ” denotes  
531 the complex conjugate and  $\Lambda$  is a  $4D \times 4D$  diagonal matrix containing the eigenvalues of  $\mathbf{G}_c$ . Due to the  
532 diagonalization of the matrix  $\mathbf{G}_c$ , equation 43 can be rewritten by using equation 50 and premultiplying  
533 both sides of the result by  $(\mathcal{F}_{2D_B} \otimes \mathcal{F}_{2D_b})$ , i.e.,

$$\Lambda (\mathcal{F}_{2D_B} \otimes \mathcal{F}_{2D_b}) \mathbf{v}_c = (\mathcal{F}_{2D_B} \otimes \mathcal{F}_{2D_b}) \mathbf{w}_c. \quad (51)$$

534 By following ?, we rearrange equation 51 as follows

$$\mathcal{L} \circ (\mathcal{F}_{2D_B} \mathcal{V}_c \mathcal{F}_{2D_b}) = \mathcal{F}_{2D_B} \mathcal{W}_c \mathcal{F}_{2D_b} \quad (52)$$

535 where “ $\circ$ ” denotes the Hadamard product (e.g., ?, p. 298) and  $\mathcal{L}$ ,  $\mathcal{V}_c$  and  $\mathcal{W}_c$  are  $2D_B \times 2D_b$  matrices  
 536 obtained by rearranging, along their rows, the elements forming the diagonal of  $\Lambda$  (equation 50), vector  $\mathbf{v}_c$   
 537 and vector  $\mathbf{w}_c$  (equation 44), respectively. Then, by premultiplying both sides of equation 52 by  $\mathcal{F}_{2D_B}^*$  and  
 538 then postmultiplying both sides by  $\mathcal{F}_{2D_b}^*$ , we obtain

$$\mathcal{F}_{2D_B}^* [\mathcal{L} \circ (\mathcal{F}_{2D_B} \mathcal{V}_c \mathcal{F}_{2D_b})] \mathcal{F}_{2D_b}^* = \mathcal{W}_c. \quad (53)$$

539 Finally, we get from equation 50 that matrix  $\mathcal{L}$  can be computed by using only the first column  $\mathbf{G}_c[:, 1]$  of  
 540 the BCCB matrix  $\mathbf{G}_c$  (equation 43) according to (?)

$$\mathcal{L} = \sqrt{4D} \mathcal{F}_{2D_B} \mathcal{C} \mathcal{F}_{2D_b}, \quad (54)$$

541 where  $\mathcal{C}$  is a  $2D_B \times 2D_b$  matrix obtained by rearranging, along its rows, the elements of  $\mathbf{G}_c[:, 1]$  (equation  
 542 43).

543 The whole procedure to compute the original matrix-vector products  $\mathbf{G}\mathbf{v}$  (equation 40) and  $\mathbf{G}^\top\mathbf{v}$   
 544 (equation 41) consists in (i) rearranging the elements of the vector  $\mathbf{v}$  and the first column  $\mathbf{G}[:, 1]$  of matrix  
 545  $\mathbf{G}$  into the matrices  $\mathcal{V}_c$  and  $\mathcal{C}$  (equations 53 and 54), respectively; (ii) computing terms  $\mathcal{F}_{2D_B} \mathcal{A} \mathcal{F}_{2D_b}$  and  
 546  $\mathcal{F}_{2D_B}^* \mathcal{A} \mathcal{F}_{2D_b}^*$ , where  $\mathcal{A}$  is a given matrix, and a Hadamard product to obtain  $\mathcal{W}_c$  (equation 53); and (iii)  
 547 retrieve the elements of vector  $\mathbf{w}$  (equation 40) from  $\mathcal{W}_c$  (equation 53). It is important noting that the steps  
 548 (i) and (iii) do not have any computational cost because they involve only reorganizing elements of vectors  
 549 and matrices. Besides, the terms  $\mathcal{F}_{2D_B} \mathcal{A} \mathcal{F}_{2D_b}$  and  $\mathcal{F}_{2D_B}^* \mathcal{A} \mathcal{F}_{2D_b}^*$  in step (ii) represent, respectively, the  
 550 2D Discrete Fourier Transform (2D-DFT) and the 2D Inverse Discrete Fourier Transform (2D-IDFT) of  $\mathcal{A}$ .  
 551 These transforms can be efficiently computed by using the 2D Fast Fourier Transform (2D-FFT). Hence,  
 552 the original matrix-vector products  $\mathbf{G}\mathbf{v}$  (equation 40) and  $\mathbf{G}^\top\mathbf{v}$  (equation 41) can be efficiently computed  
 553 by using the 2D-FFT.

554 PAREI AQUI: É NECESSÁRIO FALAR QUE A PARTIR DE  $\mathbf{G}[:, 1]$  É POSSÍVEL OBTER  $\mathbf{G}^T[:, 1]$   
 555 SABENDO-SE O TIPO DE SIMETRIA DA ESTRUTURA BTTB. ISSO POSSIBILITA USAR  $\mathbf{G}[:, 1]$   
 556 DEFINIR A  $\mathbf{G}_c[:, 1]$  ASSOCIADA AO PRODUTO  $\mathbf{G}\mathbf{v} = \mathbf{w}$  OU AO PRODUTO  $\mathbf{G}^\top\mathbf{v} = \mathbf{w}$

## 5 SOLUTION STABILITY

557 The solution stability of the equivalent-layer methods is rarely addressed. Here, we follow the numerical  
 558 stability analysis presented in Siqueira et al. (2017).

559 Let us assume noise-free potential-field data  $\mathbf{d}$ , we estimate a physical-property distribution  $\mathbf{p}$  (estimated  
 560 solution) within the equivalent layer. Then, the noise-free data  $\mathbf{d}$  are contaminated with additive  $D$  different  
 561 sequences of pseudorandom Gaussian noise, creating different noise-corrupted potential-field data  $\mathbf{d}_\ell^0$ ,  
 562  $\ell = 1, \dots, D$ . From each  $\mathbf{d}_\ell^0$ , we estimate a physical-property distribution  $\hat{\mathbf{p}}_\ell$  within the equivalent layer.

563 Next, for each noise-corrupted data  $\mathbf{d}_\ell^0$  and estimated solution  $\hat{\mathbf{p}}_\ell$ , the  $\ell$ th model perturbation  $\delta p_\ell$  and the  
 564  $\ell$ th data perturbation  $\delta d_\ell$  are, respectively, evaluated by

$$\delta p_\ell = \frac{\|\hat{\mathbf{p}}_\ell - \mathbf{p}\|_2}{\|\mathbf{p}\|_2}, \quad \ell = 1, \dots, D, \quad (55)$$

565 and

$$\delta d_\ell = \frac{\|\mathbf{d}_\ell^0 - \mathbf{d}\|_2}{\|\mathbf{d}\|_2}, \quad \ell = 1, \dots, D. \quad (56)$$

**Algorithm 6:** Generic pseudo-code for the convolutional equivalent-layer method proposed by ??.**Initialization :**


---

```

1 Set the regular grid of  $P$  equivalent sources on a horizontal plane  $z_0$  ;
2 Set a tolerance  $\epsilon$  and a maximum number of iterations ITMAX ;
3 Compute the first column  $\mathbf{G}[:, 1]$  of the sensitivity matrix  $\mathbf{G}$  (equation 58) for the particular case in
   which it has a BTTB structure (equation 39);
4 Rearrange the elements of  $\mathbf{G}[:, 1]$  into the first column  $\mathbf{G}_c[:, 1]$  of the BCCB matrix  $\mathbf{G}_c$  (equation 43);
5 Rearrange  $\mathbf{G}_c[:, 1]$  to obtain  $\mathcal{C}$  (equation 54);
6 Compute  $\mathcal{F}_{2D_B} \mathcal{C} \mathcal{F}_{2D_b}$  by using a 2D Fast Fourier Transform (2D-FFT) and multiply by  $\sqrt{4D}$  to
   obtain  $\mathcal{L}$  (equation 54);
7 Set  $\tilde{\mathbf{p}} = \mathbf{0}$  ;
8 Set  $\mathbf{r} = \mathbf{d}$  and compute  $\delta = \|\mathbf{r}\|/D$  ;
9 Compute  $\vartheta = \mathbf{G}^\top \mathbf{r}$  (Algorithm 7) and  $\rho_0 = \vartheta^\top \vartheta$  ;
10 Set  $\tau = 0$  and  $\eta = \mathbf{0}$  ;
11  $m = 1$  ;
12 while ( $\delta > \epsilon$ ) and ( $m < \text{ITMAX}$ ) do
13   Update  $\eta \leftarrow \vartheta + \tau \eta$  ;
14   Compute  $\nu = \mathbf{G} \eta$  (Algorithm 7);
15   Compute  $v = \rho_0 / (\nu^\top \nu)$  ;
16   Update  $\tilde{\mathbf{p}} \leftarrow \tilde{\mathbf{p}} + v \eta$  ;
17   Update  $\mathbf{r} \leftarrow \mathbf{r} - v \nu$  and compute  $\delta \leftarrow \|v \nu\|/D$  ;
18   Compute  $\vartheta = \mathbf{G}^\top \mathbf{r}$  (Algorithm 7) and  $\rho = \vartheta^\top \vartheta$  ;
19   Compute  $\tau = \rho / \rho_0$  ;
20   Update  $\rho_0 \leftarrow \rho$  ;
21    $m \leftarrow m + 1$  ;
22 end

```

---

**Algorithm 7:** Pseudo-code for computing the generic matrix-vector product given by equation 40
via fast 2D discrete convolution.

---

```

1 Rearrange  $\mathbf{v}$  (equations 40 and 42) into  $\mathbf{v}_c$  (equations 43–45);
2 Rearrange  $\mathbf{v}_c$  into  $\mathcal{V}_c$ , compute  $\mathcal{F}_{2D_B} \mathcal{V}_c \mathcal{F}_{2D_b}$  via 2D-FFT and evaluate its Hadamard product with
   matrix  $\mathcal{L}$  to define an auxiliary matrix  $\mathcal{A} = \mathcal{L} \circ (\mathcal{F}_{2D_B} \mathcal{V}_c \mathcal{F}_{2D_b})$ ;
3 Compute  $\mathcal{F}_{2D_B}^* \mathcal{A} \mathcal{F}_{2D_b}^*$  via 2D-FFT inverse to evaluate  $\mathcal{W}_c$  (equation 53);
4 Retrieve  $\mathbf{w}_c$  (equations 43–45) from  $\mathcal{W}_c$  (equation 53);
5 Retrieve  $\mathbf{w}$  (equations 40 and 42) from  $\mathbf{w}_c$  (equations 43–45);

```

---

566 Regardless of the particular method used, the following inequality (Aster et al., 2018, p. 66) is applicable:

$$\delta p_\ell \leq \kappa \delta d_\ell, \quad \ell = 1, \dots, D, \quad (57)$$

567 where  $\kappa$  is the constant of proportionality between the model perturbation  $\delta p_\ell$  (equation 84) and the data  
568 perturbation  $\delta d_\ell$  (equation 85). The constant  $\kappa$  acts as the condition number of an invertible matrix in a  
569 given inversion, and thus measures the instability of the solution. The larger (smaller) the value of  $\kappa$  the  
570 more unstable (stable) is the estimated solution.

571 Equation 86 shows a linear relationship between the model perturbation and the data perturbation. By  
572 plotting  $\delta p_\ell$  (equation 84) against  $\delta d_\ell$  (equation 85) produced by a set of  $D$  estimated solution obtained by  
573 applying a given equivalent-layer method, we obtain a straight line behaviour described by equation 86.

574 By applying a linear regression, we obtain a fitted straight line whose estimated slope ( $\kappa$  in equation 86)  
 575 quantifies the solution stability.

576 Here, the analysis of solution stability is numerically conducted by applying the classical equivalent-  
 577 layer technique with zeroth-order Tikhonov regularization, the convolutional method for gravimetric and  
 578 magnetic data, the deconvolutional method (equation 82) and the deconvolutional method with different  
 579 values for the Wiener stabilization (equation 83).

## 6 THE EQUIVALENT-LAYER TECHNIQUE

### 580 6.1 Fundamentals

581 Consider a set of  $N$  potential-field observations (gravity or magnetic data)  $d_i^o (x_i, y_i, z_i)$ ,  $i = 1, \dots, N$ ,  
 582 at the  $i$ th observation point  $(x_i, y_i, z_i)$  of a Cartesian coordinate system with  $x$ -,  $y$ - and  $z$ -axis pointing to  
 583 north, east and down, respectively. Physically, the discrete set of potential-field observations is produced by  
 584 a unknown source distribution in the subsurface. Mathematically, it represents a discrete set of a harmonic  
 585 function.

586 A standard way to deal with the classical equivalent-layer technique is approximate the observed potential-  
 587 field data by the predicted data, which in turn are produced by a fictitious layer of sources, called equivalent  
 588 layer. The equivalent layer is located below the observation surface, at depth  $z_0$  ( $z_0 > z_i$ ), and with finite  
 589 horizontal dimensions being composed by a finite discrete set of equivalent sources (e.g., point masses,  
 590 dipoles, or prisms). Mathematically, this approximation can be written in matrix notation as

$$\mathbf{d} = \mathbf{Ap}, \quad (58)$$

591 where  $\mathbf{d}$  is an  $N$ -dimensional predicted data vector whose  $i$ th element,  $d_i (x_i, y_i, z_i)$ ,  $i = 1, \dots, N$ , is the  
 592 predicted potential-field observation,  $\mathbf{p}$  is an  $M$ -dimensional parameter vector whose  $j$ th element  $p_j$  can be  
 593 a physical property of the  $j$ th equivalent source and  $\mathbf{A}$  is the  $N \times M$  sensitivity matrix whose  $ij$ th element  
 594  $a_{ij}$  is a harmonic function.

### 595 6.2 Computational strategies

596 The classical equivalent-layer technique consists of estimating the parameter vector  $\mathbf{p}$  from the  $N$ -  
 597 dimensional observed data vector  $\mathbf{d}^o$  whose  $i$ th element is defined as the  $d_i^o (x_i, y_i, z_i)$ ,  $i = 1, \dots, N$ .  
 598 Usually, this estimate can be obtained by a regularized least-squares solution. The estimated parameter  
 599 is stable, fits the observed data and can be used to yield a desired linear transformation of the data, such  
 600 as interpolation, upward (or downward) continuation, reduction to the pole, joint processing of gravity  
 601 gradient data and more. Mathematically, the desired linear transformation of the data can be obtained by

$$\hat{\mathbf{t}} = \mathbf{T}\mathbf{p}^*, \quad (59)$$

602 where  $\hat{\mathbf{t}}$  is an  $N$ -dimensional transformed data vector,  $\mathbf{p}^*$  is an  $M$ -dimensional estimated parameter vector  
 603 and  $\mathbf{T}$  is the  $N \times M$  matrix of Green's functions whose  $ij$ th element is the transformed field at the  $i$ th  
 604 observation point produced by the  $j$ th equivalent source.

605 The biggest hurdle to use the classical equivalent-layer technique is the computational complexity to  
 606 handle large datasets because the sensitivity matrix  $\mathbf{A}$  (equation 58) is dense. Usually, the estimated  
 607 parameter vector  $\mathbf{p}^*$  requires to solve a large-scale linear inversion which in turn means to deal with

608 some obstacles concerning large computational cost: i) the large computer memory to store large and full  
 609 matrices; ii) the long computation time to multiply a matrix by a vector; and iii) the long computation time  
 610 to solve a large linear system of equations.

611 Here, we review some strategies for reducing the computational cost of equivalent-layer technique. These  
 612 strategies are the following:

### 613 6.2.1 The moving data-window scheme

614 Leão and Silva (1989) reduced the total processing time and memory usage of equivalent-layer technique  
 615 by means of a moving data-window scheme. A small moving data window with  $N_w$  observations and  
 616 a small equivalent layer with  $M_w$  equivalent sources ( $M_w > N_w$ ) located below the observations are  
 617 established. For each position of a moving-data window, Leão and Silva (1989) estimate a stable solution  
 618  $\mathbf{p}_w^*$  by using a data-space approach with the zeroth-order Tikhonov regularization (Aster et al., 2018), i.e.,

$$(A_w A_w^\top + \mu I) w = d_w^o, \quad (60a)$$

$$A_w^\top w = p_w^*, \quad (60b)$$

619 where  $w$  is a dummy vector,  $\mu$  is a regularizing parameter,  $d_w^o$  is an  $N_w$ -dimensional vector containing  
 620 the observed potential-field data,  $A_w$  is an  $N_w \times M_w$  sensitivity matrix related to a moving-data window,  $I$   
 621 is an identity matrix of order  $N_w$  and the superscript  $\top$  stands for a transpose. After estimating an  $M_w \times 1$   
 622 parameter vector  $p_w^*$  (equation 60b) the desired transformation of the data is only calculated at the central  
 623 point of each moving-data window, i.e.:

$$\hat{t}_k = t_k^\top p_w^*, \quad (61)$$

624 where  $\hat{t}_k$  is the transformed data calculated at the central point  $k$  of the data window and  $t_k$  is an  $M_w \times 1$   
 625 vector whose elements form the  $k$ th row of the  $N_w \times N_w$  matrix of Green's functions  $T$  (equation 59) of  
 626 the desired linear transformation of the data.

627 By shifting the moving-data window with a shift size of one data spacing, a new position of a data  
 628 window is set up. Next, the aforementioned process (equations 60b and 61) is repeated for each position of  
 629 a moving-data window, until the entire data have been processed. Hence, instead of solving a large inverse  
 630 problem, Leão and Silva (1989) solve several much smaller ones.

631 To reduce the size of the linear system to be solved, Soler and Uieda (2021) adopted the same strategy  
 632 proposed, originally, by Leão and Silva (1989) of using a small moving-data window sweeping the whole  
 633 data. In Leão and Silva (1989), a moving-data window slides to the next adjacent data window following a  
 634 sequential movement, the predicted data is calculated inside the data window and the desired transformation  
 635 are only calculated at the center of the moving-data window. Unlike Leão and Silva (1989), Soler and  
 636 Uieda (2021) do not adopt a sequential order of the data windows; rather, they adopt a randomized  
 637 order of windows in the iterations of the gradient-boosting algorithm (Friedman, 2001 and 2002). The  
 638 gradient-boosting algorithm in Soler and Uieda (2021) estimates a stable solution using the data and the  
 639 equivalent sources that fall within a moving-data window; however, it calculates the predicted data and the  
 640 residual data in the whole survey data. Next, the residual data that fall within a new position of the data  
 641 window is used as input data to estimate a new stable solution within the data window which in turn is  
 642 used to calculate a new predicted data and a new residual data in the whole survey data. Finally, unlike  
 643 Leão and Silva (1989), in Soler and Uieda (2021) neither the data nor the equivalent sources need to be  
 644 distributed in regular grids. Indeed, Leão and Silva (1989) built their method using regular grids, but in fact

regular grids are not necessary. Regarding the equivalent-source layout, Soler and Uieda (2021) proposed the block-averaged sources locations in which the survey area is divided into horizontal blocks and one single equivalent source is assigned to each block. Each single source per block is placed over the layer with its horizontal coordinates given by the average horizontal positions of observation points. According to Soler and Uieda (2021), the block-averaged sources layout reduces the number of equivalent sources significantly and the gradient-boosting algorithm provides even greater efficiency in terms of data fitting.

### 651 6.2.2 The equivalent-data concept

652 To reduced the total processing time and memory usage of equivalent-layer technique, Mendonça and  
 653 Silva (1994) proposed a strategy called 'equivalent data concept'. The equivalent data concept is grounded  
 654 on the principle that there is a subset of redundant data that does not contribute to the final solution and  
 655 thus can be dispensed. Conversely, there is a subset of observations, called equivalent data, that contributes  
 656 effectively to the final solution and fits the remaining observations (redundant data). Iteratively, Mendonça  
 657 and Silva (1994) selected the subset of equivalent data that is substantially smaller than the original dataset.  
 658 This selection is carried out by incorporating one data point at a time.

659 According to Mendonça and Silva (1994), the number of equivalent data is about one-tenth of the total  
 660 number of observations. These authors used the equivalent data concept to carry out an interpolation of  
 661 gravity data. They showed a reduction of the total processing time and memory usage by, at least, two  
 662 orders of magnitude as opposed to using all observations in the interpolation process via the classical  
 663 equivalent-layer technique.

### 664 6.2.3 The wavelet compression and lower-dimensional subspace

665 For large data sets, the sensitivity matrix  $\mathbf{A}$  (equation 58) is a drawback in applying the equivalent-layer  
 666 technique because it is a large and dense matrix.

667 Li and Oldenburg (2010) transformed a large and full sensitivity matrix into a sparse one by using fast  
 668 wavelet transforms. In the wavelet domain, Li and Oldenburg (2010) applyied a 2D wavelet transform to  
 669 each row and column of the original sensitivity matrix  $\mathbf{A}$  to expand it in the wavelet bases. This operation  
 670 can be done by premultiplying the original sensitivity matrix  $\mathbf{A}$  by a matrix representing the 2D wavelet  
 671 transform  $\mathbf{W}_2$  and then the resulting is postmultiplied by the transpose of  $\mathbf{W}_2$  (i.e.,  $\mathbf{W}_2^\top$ ).

$$\tilde{\mathbf{A}} = \mathbf{W}_2 \mathbf{A} \mathbf{W}_2^\top, \quad (62)$$

672 where  $\tilde{\mathbf{A}}$  is the expanded original sensitivity matrix in the wavelet bases with many elements zero or close  
 673 to zero. Next, the matrix  $\tilde{\mathbf{A}}$  is replaced by its sparse version  $\tilde{\mathbf{A}}_s$  in the wavelet domain which in turn is  
 674 obtained by retaining only the large elements of the  $\tilde{\mathbf{A}}$ . Thus, the elements of  $\tilde{\mathbf{A}}$  whose amplitudes fall  
 675 below a relative threshold are discarded. In Li and Oldenburg (2010), the original sensitivity matrix  $\mathbf{A}$   
 676 is high compressed resulting in a sparce matrix  $\tilde{\mathbf{A}}_s$  with a few percent of nonzero elements and the the  
 677 inverse problem is solved in the wavelet domain by using  $\tilde{\mathbf{A}}_s$  and a incomplete conjugate gradient least  
 678 squares, without an explicit regularization parameter and a limited number of iterations. The solution is  
 679 obtained by solving the following linear system

$$\tilde{\mathbf{A}}_L^\top \tilde{\mathbf{A}}_L \tilde{\mathbf{p}}_L^* = \tilde{\mathbf{A}}_L^\top \tilde{\mathbf{d}}^o, \quad (63)$$

680 where  $\tilde{\mathbf{p}}_L^*$  is obtained by solving the linear system given by equation 63,

$$\tilde{\mathbf{A}}_L = \tilde{\mathbf{A}}_s \tilde{\mathbf{L}}^{-1}, \quad (64a)$$

$$\tilde{\mathbf{p}}_L = \tilde{\mathbf{L}} \tilde{\mathbf{p}}, \quad (64b)$$

$$\tilde{\mathbf{d}}^o = \mathbf{W}_2 \mathbf{d}^o, \quad (64c)$$

681 where  $\tilde{\mathbf{L}}$  is a diagonal and invertible weighting matrix representing the finite-difference approximation in  
682 the wavelet domain. Finally, the distribution over the equivalent layer in the space domain  $\mathbf{p}$  is obtained by  
683 applying an inverse wavelet transform in two steps, i.e.:

$$\tilde{\mathbf{p}} = \tilde{\mathbf{L}}^{-1} \tilde{\mathbf{p}}_L^*, \quad (65)$$

684 and

$$\mathbf{p} = \mathbf{W}_2 \tilde{\mathbf{p}}. \quad (66)$$

685 Although the data misfit quantifying the difference between the observed and predicted data by the  
686 equivalent source is calculated in the wavelet domain, we understand that the desired transformation is  
687 calculated via equation 59 which uses a full matrix of Green's functions  $\mathbf{T}$ .

688 Li and Oldenburg (2010) used the equivalent-layer technique with a wavelet compression to perform an  
689 upward continuation of total-field anomaly between uneven surfaces. For regularly spaced grid of data, Li  
690 and Oldenburg (2010) reported that high compression ratios are achieved with insignificant loss of accuracy.  
691 As compared to the upward-continued total-field anomaly by equivalent layer using the dense matrix, Li  
692 and Oldenburg's (2010) approach, using the Daubechies wavelet, decreased CPU (central processing unit)  
693 time by up to two orders of magnitude.

694 Mendonça (2020) overcame the solution of intractable large-scale equivalent-layer problem by using the  
695 subspace method (e.g., Skilling and Bryan, 1984; Kennett et al., 1988; Oldenburg et al., 1993; Barbosa  
696 et al., 1997). The subspace method reduces the dimension of the linear system of equations to be solved.  
697 Given a higher-dimensional space (e.g.,  $M$ -dimensional model space,  $\mathbb{R}^M$ ), there exists many lower-  
698 dimensional subspaces (e.g.,  $Q$ -dimensional subspace) of  $\mathbb{R}^M$ . The linear inverse problem related to the  
699 equivalent-layer technique consists in finding an  $M$ -dimension parameter vector  $\mathbf{p} \in \mathbb{R}^M$  which adequately  
700 fits the potential-field data. The subspace method looks for a parameter vector who lies in a  $Q$ -dimensional  
701 subspace of  $\mathbb{R}^M$  which, in turn, is spanned by a set of  $Q$  vectors  $\mathbf{v}_i = 1, \dots, Q$ , where  $\mathbf{v}_i \in \mathbb{R}^M$ . In matrix  
702 notation, the parameter vector in the subspace method can be written as

$$\mathbf{p} = \mathbf{V} \boldsymbol{\alpha}, \quad (67)$$

703 where  $\mathbf{V}$  is an  $M \times Q$  matrix whose columns  $\mathbf{v}_i = 1, \dots, Q$  form a basis vectors for a subspace  $Q$  of  $\mathbb{R}^M$ .  
704 In equation 67, the parameter vector  $\mathbf{p}$  is defined as a linear combination in the space spanned by  $Q$  basis  
705 vectors  $\mathbf{v}_i = 1, \dots, Q$  and  $\boldsymbol{\alpha}$  is a  $Q$ -dimensional unknown vector to be determined. The main advantage of  
706 the subspace method is that the linear system of  $M$  equations in  $M$  unknowns to be originally solved is  
707 reduced to a new linear system of  $Q$  equations in  $Q$  unknowns which requires much less computational  
708 effort since  $Q \ll M$ , i.e.:

$$\mathbf{V}^\top \mathbf{A}^\top \mathbf{A} \mathbf{V} \boldsymbol{\alpha}^* = \mathbf{V}^\top \mathbf{d}^o. \quad (68)$$

709 To avoid the storage of matrices  $\mathbf{A}$  and  $\mathbf{V}$ , Mendonça (2020) evaluates an element of the matrix  $\mathbf{AV}$  by  
710 calculating the dot product between the row of matrix  $\mathbf{A}$  and the column of the matrix  $\mathbf{B}$ . After estimating

711  $\alpha^*$  (equation 68) belonging to a  $Q$ -dimensional subspace of  $\mathbb{R}^M$ , the distribution over the equivalent layer  
 712  $\mathbf{p}$  in the  $\mathbb{R}^M$  is obtained by applying equation 67. The choice of the  $Q$  basis vectors  $\mathbf{v}_i = 1, \dots, Q$  (equation  
 713 67) in the subspace method is not strict. Mendonça (2020), for example, chose the eigenvectors yielded by  
 714 applying the singular value decomposition of the matrix containing the gridded data set. The number of  
 715 eigenvectors used to form basis vectors will depend on the singular values.

716 The proposed subspace method for solving large-scale equivalent-layer problem by Mendonça (2020)  
 717 was applied to estimate the mass excess or deficiency caused by causative gravity sources.

#### 718 6.2.4 The quadtree discretization

719 To make the equivalent-layer technique tractable, Barnes and Lumley (2011) also transformed the dense  
 720 sensitivity matrix  $\mathbf{A}$  (equation 58) into a sparse matrix. In Barnes and Lumley (2011), a sparse version of  
 721 the sensitivity matrix is achieved by grouping equivalent sources (e.g., they used prisms) distant from an  
 722 observation point together to form a larger prism or larger block. Each larger block has averaged physical  
 723 properties and averaged top- and bottom-surfaces of the grouped smaller prisms (equivalent sources) that  
 724 are encompassed by the larger block. The authors called it the 'larger averaged block' and the essence of  
 725 their method is the reduction in the number of equivalent sources, which means a reduction in the number  
 726 of parameters to be estimated implying in model dimension reduction.

727 The key of the Barnes and Lumley's (2011) method is the algorithm for deciding how to group the smaller  
 728 prisms. In practice, these authors used a recursive bisection process that results in a quadtree discretization  
 729 of the equivalent-layer model.

730 By using the quadtree discretization, Barnes and Lumley (2011) were able to jointly process multiple  
 731 components of airborne gravity-gradient data using a single layer of equivalent sources. To our knowledge,  
 732 Barnes and Lumley (2011) are the pioneers on processing full-tensor gravity-gradient data jointly. In  
 733 addition to computational feasibility, Barnes and Lumley's (2011) method reduces low-frequency noise  
 734 and can also remove the drift in time-domain from the survey data. Those authors stressed that the  
 735  $G_{zz}$ -component calculated through the single estimated equivalent-layer model projected on a grid at a  
 736 constant elevation by inverting full gravity-gradient data has the low-frequency error reduced by a factor of  
 737 2.4 as compared to the inversion of an individual component of the gravity-gradient data.

#### 738 6.2.5 The reparametrization of the equivalent layer

739 Oliveira Jr. et al. (2013) reparametrized the whole equivalent-layer model by a piecewise bivariate-  
 740 polynomial function defined on a set of  $Q$  equivalent-source windows. In Oliveira Jr. et al.'s (2013)  
 741 approach, named polynomial equivalent layer (PEL), the parameter vector within the  $k$ th equivalent-source  
 742 window  $\mathbf{p}^k$  can be written in matrix notation as

$$\mathbf{p}^k = \mathbf{B}^k \mathbf{c}^k, \quad k = 1 \dots Q, \quad (69)$$

743 where  $\mathbf{p}^k$  is an  $M_w$ -dimensional vector containing the physical-property distribution within the  $k$ th  
 744 equivalent-source window,  $\mathbf{c}^k$  is a  $P$ -dimensional vector whose  $l$ th element is the  $l$ th coefficient of the  
 745  $\alpha$ th-order polynomial function and  $\mathbf{B}^k$  is an  $M_w \times P$  matrix containing the first-order derivative of the  
 746  $\alpha$ th-order polynomial function with respect to one of the  $P$  coefficients.

747 By using a regularized potential-field inversion, Oliveira Jr. et al. (2013) estimates the polynomial  
 748 coefficients for each equivalent-source window by solving the following linear system

$$\left( \mathbf{B}^\top \mathbf{A}^\top \mathbf{A} \mathbf{B} + \mu \mathbf{I} \right) \mathbf{c}^* = \mathbf{B}^\top \mathbf{A}^\top \mathbf{d}^o, \quad (70)$$

749 where  $\mu$  is a regularizing parameter,  $\mathbf{c}^*$  is an estimated  $H$ -dimensional vector containing all coefficients  
 750 describing all polynomial functions within all equivalent-source windows which compose the entire  
 751 equivalent layer,  $\mathbf{I}$  is an identity matrix of order  $H$  ( $H = P\bar{Q}$ ) and  $\mathbf{B}$  is an  $M \times H$  block diagonal matrix  
 752 such that the main-diagonal blocks are  $\mathbf{B}^k$  matrices (equation 69) and all off-diagonal blocks are zero  
 753 matrices. For ease of the explanation of equation 70, we keep only the zeroth-order Tikhonov regularization  
 754 and omitting the first-order Tikhonov regularization (Aster et al., 2018) which was also used by Oliveira Jr.  
 755 et al. (2013).

756 The main advantage of the PEL is solve  $H$ -dimensional system of equations (equation 70), where  $H$   
 757 totalizes the number of polynomial coefficients composing all equivalent-source windows, requiring a  
 758 lower computational effort since  $H << N$ . To avoid the storage of matrices  $\mathbf{A}$  and  $\mathbf{B}$ , Oliveira Jr. et al.  
 759 (2013) evaluate an element of the matrix  $\mathbf{AB}$  by calculating the dot product between the row of matrix  $\mathbf{A}$   
 760 and the column of the matrix  $\mathbf{B}$ . After estimating all polynomial coefficients of all windows, the estimated  
 761 coefficients ( $\mathbf{c}^*$  in equation 70) are transformed into a single physical-property distribution encompassing  
 762 the entire equivalent layer.

763 As stated by Oliveira Jr. et al. (2013), the computational efficiency of PEL approach stems from the fact  
 764 that the total number of polynomial coefficients  $H$  required to depict the physical-property distribution  
 765 within the equivalent layer is generally much smaller than the number of equivalent sources. Consequently,  
 766 this leads to a considerably smaller linear system that needs to be solved. Hence, the main strategy of  
 767 polynomial equivalent layer is the model dimension reduction.

768 The polynomial equivalent layer was applied to perform upward continuations of gravity and magnetic  
 769 data and reduction to the pole of magnetic data.

#### 770 6.2.6 The iterative scheme without solving a linear system

771 There exists a class of methods that iteratively estimate the distribution of physical properties within an  
 772 equivalent layer without the need to solve linear systems. The method initially introduced by Cordell (1992)  
 773 and later expanded upon by Guspi and Novara (2009) updates the physical property of sources, located  
 774 beneath each potential-field data, by removing the maximum residual between the observed and fitted data.  
 775 In addition, Xia and Sprowl (1991) and Xia et al. (1993) have developed efficient iterative algorithms for  
 776 updating the distribution of physical properties within the equivalent layer in the wavenumber and space  
 777 domains, respectively. Specifically, in Xia and Sprowl's (1991) method the physical-property distribution is  
 778 updated by using the ratio between the squared depth to the equivalent source and the gravitational constant  
 779 multiplied by the residual between the observed and predicted observation at the measurement station.  
 780 Neither of these methods solve linear systems.

781 Following this class of methods of iterative equivalent-layer technique that does not solve linear systems,  
 782 Siqueira et al. (2017) developed a fast iterative equivalent-layer technique for processing gravity data in  
 783 which the sensitivity matrix  $\mathbf{A}$  (equation 58) is replaced by a diagonal matrix  $N \times N$ , i.e.:

$$\tilde{\mathbf{A}} = 2\pi\gamma\Delta\mathbf{S}^{-1}, \quad (71)$$

where  $\gamma$  is Newton's gravitational constant and  $\Delta S^{-1}$  is a diagonal matrix of order  $N$  whose diagonal elements  $\Delta s_i$ ,  $i = 1, \dots, N$  are the element of area centered at the  $i$ th horizontal coordinates of the  $i$ th observation point. The physical foundations of Siqueira et al.'s (2017) method rely on two constraints: i) the excess of mass; and ii) the positive correlation between the gravity observations and the mass distribution over the equivalent layer.

Although Siqueira et al.'s (2017) method does not solve any linear system of equations, it can be theoretically explained by solving the following linear system at the  $k$ th iteration:

$$\tilde{\mathbf{A}}^\top \tilde{\mathbf{A}} \Delta \hat{\mathbf{p}}^k = \tilde{\mathbf{A}}^\top \mathbf{r}^k, \quad (72)$$

where  $\mathbf{r}^k$  is an  $N$ -dimensional residual vector whose  $i$ th element is calculated by subtracting the  $i$ th observed data  $d_i^o$  from the  $i$ th fitted data  $d_i^k$  at the  $k$ th iteration, i.e.,

$$r_i^k = d_i^o - d_i^k. \quad (73)$$

and  $\Delta \hat{\mathbf{p}}^k$  is an estimated  $N$ -dimensional vector of parameter correction.

Because  $\tilde{\mathbf{A}}$ , in equation 72, is a diagonal matrix (equation 71), the parameter correction estimate is directly calculated without solving system of linear equations, and thus, an  $i$ th element of  $\Delta \hat{\mathbf{p}}^k$  is directly calculated by

$$\Delta \hat{p}_i^k = \frac{\Delta s_i r_i^k}{2 \pi \gamma}. \quad (74)$$

The mass distribution over the equivalent layer is updated by:

$$\hat{p}_i^{k+1} = \hat{p}_i^k + \Delta \hat{p}_i^k. \quad (75)$$

Siqueira et al.'s (2017) method starts from a mass distribution on the equivalent layer, whose  $i$ th mass  $p_i^o$  is proportional to the  $i$ th observed data  $d_i^o$ , i.e.,

$$p_i^o = \frac{\Delta s_i d_i^o}{2 \pi \gamma}. \quad (76)$$

Siqueira et al. (2017) applied their fast iterative equivalent-layer technique to interpolate, calculate the horizontal components, and continue upward (or downward) gravity data.

For jointly process two gravity gradient components, Jirigalatu and Ebbing (2019) used the Gauss-FFT for forward calculation of potential fields in the wavenumber domain combined with Landweber's iteration coupled with a mask matrix  $\mathbf{M}$  to reduce the edge effects without increasing the computation cost. The mask matrix  $\mathbf{M}$  is defined in the following way: if the corresponding pixel does not contain the original data, the element of  $\mathbf{M}$  is set to zero; otherwise, it is set to one. The  $k$ th Landweber iteration is given by

$$\mathbf{p}_{k+1} = \mathbf{p}_k + \omega \left[ \mathbf{A}_1^\top (\mathbf{d}_1 - \mathbf{M} \mathbf{A}_1 \mathbf{p}_k) + \mathbf{A}_2^\top (\mathbf{d}_2 - \mathbf{M} \mathbf{A}_2 \mathbf{p}_k) \right], \quad (77)$$

where  $\omega$  is a relaxation factor,  $\mathbf{d}_1$  and  $\mathbf{d}_2$  are the two gravity gradient components and  $\mathbf{A}_1$  and  $\mathbf{A}_2$  are the corresponding gravity gradient kernels. Jirigalatu and Ebbing (2019) applied their method for processing two horizontal curvature components of Falcon airborne gravity gradient.

810 6.2.7 The convolutional equivalent layer with BTTB matrices

811 Takahashi et al. (2020, 2022) introduced the convolutional equivalent layer for gravimetric and magnetic  
812 data processing, respectively.

813 Takahashi et al. (2020) demonstrated that the sensitivity matrix  $\mathbf{A}$  (equation 58) associated with a planar  
814 equivalent layer formed by a set of point masses, each one directly beneath each observation point and  
815 considering a regular grid of observation points at a constant height has a symmetric block-Toeplitz Toeplitz-  
816 block (BTTB) structure. A symmetric BTTB matrix has, at least, two attractive properties. The first one is  
817 that it can be defined by using only the elements forming its first column (or row). The second attractive  
818 property is that any BTTB matrix can be embedded into a symmetric Block-Circulant Circulant-Block  
819 (BCCB) matrix. This means that the full sensitivity matrix  $\mathbf{A}$  (equation 58) can be completely reconstruct  
820 by using the first column of the BCCB matrix only. In what follows, Takahashi et al. (2020) computed  
821 the forward modeling by using only a single equivalent source. Specifically, it is done by calculating the  
822 eigenvalues of the BCCB matrix that can be efficiently computed by using only the first column of the  
823 BCCB matrix via 2D fast Fourier transform (2D FFT). By comparing with the classic approach in the  
824 Fourier domain, the convolutional equivalent layer for gravimetric data processing proposed by Takahashi  
825 et al. (2020) performed upward- and downward-continue gravity data with a very small border effects and  
826 noise amplification.

827 By using the original idea of the convolutional equivalent layer proposed by Takahashi et al. (2020)  
828 for gravimetric data processing, Takahashi et al. (2022) developed the convolutional equivalent layer for  
829 magnetic data processing. By assuming a regularly spaced grid of magnetic data at a constant height and a  
830 planar equivalent layer of dipoles, Takahashi et al. (2022) proved that the sensitivity matrix linked with  
831 this layer possess a BTTB structure in the specific scenario where each dipole is exactly beneath each  
832 observed magnetic data point. Takahashi et al. (2022) used a conjugate gradient least-squares (CGLS)  
833 algorithm which does not require an inverse matrix or matrix-matrix multiplication. Rather, it only requires  
834 matrix-vector multiplications per iteration, which can be effectively computed using the 2D FFT as a  
835 discrete convolution. The matrix-vector product only uses the elements that constitute the first column of  
836 the associated BTTB matrix, resulting in computational time and memory savings. Takahashi et al. (2022)  
837 showed the robustness of the convolutional equivalent layer in processing magnetic survey that violates the  
838 requirement of regular grids in the horizontal directions and flat observation surfaces.

839 The matrix-vector product in Takahashi et al. (2020, 2022) (e.g.,  $\mathbf{d} = \mathbf{Ap}$ , such as in equation 58) is the  
840 main issue to be solved. To solve it efficiently, these authors involved the auxiliary linear system

$$\mathbf{w} = \mathbf{Cv}, \quad (78)$$

841 where  $\mathbf{w}$  and  $\mathbf{v}$  are, respectively, vectors of data and parameters completed by zeros and  $\mathbf{C}$  is a BCCB  
842 matrix formed by  $2Q \times 2Q$  blocks, where each block  $\mathbf{C}_q$ ,  $q = 0, \dots, Q - 1$ , is a  $2P \times 2P$  circulant matrix.  
843 The first column of  $\mathbf{C}$  is obtained by rearranging the first column of the sensitivity matrix  $\mathbf{A}$  (equation 58).  
844 Because a BCCB matrix is diagonalized by the 2D unitary discrete Fourier transform (DFT),  $\mathbf{C}$  can be  
845 written as

$$\mathbf{C} = (\mathbf{F}_{2Q} \otimes \mathbf{F}_{2P})^* \boldsymbol{\Lambda} (\mathbf{F}_{2Q} \otimes \mathbf{F}_{2P}), \quad (79)$$

846 where the symbol “ $\otimes$ ” denotes the Kronecker product (Neudecker, 1969),  $\mathbf{F}_{2Q}$  and  $\mathbf{F}_{2P}$  are the  $2Q \times 2Q$   
847 and  $2P \times 2P$  unitary DFT matrices (Davis, 1979, p. 31), respectively, the superscript “ $*$ ” denotes the  
848 complex conjugate and  $\boldsymbol{\Lambda}$  is a  $4QP \times 4QP$  diagonal matrix containing the eigenvalues of  $\mathbf{C}$ . Due to the

849 diagonalization of the matrix  $\mathbf{C}$ , the auxiliary system (equation 78) can be rewritten by using equation 79  
 850 and premultiplying both sides of the result by  $(\mathbf{F}_{2Q} \otimes \mathbf{F}_{2P})$ , i.e.,

$$\Lambda (\mathbf{F}_{2Q} \otimes \mathbf{F}_{2P}) \mathbf{v} = (\mathbf{F}_{2Q} \otimes \mathbf{F}_{2P}) \mathbf{w}. \quad (80)$$

851 By applying the vec-operator (Takahashi et al., 2020) to both sides of equation 80, by premultiplying both  
 852 sides of the result by  $\mathbf{F}_{2Q}^*$  and then postmultiplying both sides of the result by  $\mathbf{F}_{2P}^*$

$$\mathbf{F}_{2Q}^* [\mathbf{L} \circ (\mathbf{F}_{2Q} \mathbf{V} \mathbf{F}_{2P})] \mathbf{F}_{2P}^* = \mathbf{W}, \quad (81)$$

853 where “ $\circ$ ” denotes the Hadamard product (Horn and Johnson, 1991, p. 298) and  $\mathbf{L}$ ,  $\mathbf{V}$  and  $\mathbf{W}$  are  $2Q \times 2P$   
 854 matrices obtained by rearranging, along their rows, the elements forming the diagonal of matrix  $\Lambda$ , vector  $\mathbf{v}$   
 855 and vector  $\mathbf{w}$ , respectively. The left side of equation 81 contains the 2D Inverse Discrete Fourier Transform  
 856 (IDFT) of the term in brackets, which in turn represents the Hadamard product of matrix  $\mathbf{L}$  and the 2D  
 857 DFT of matrix  $\mathbf{V}$ . Matrix  $\mathbf{L}$  contains the eigenvalues of  $\Lambda$  (equation 79) and can be efficiently computed  
 858 by using only the first column of the BCCB matrix  $\mathbf{C}$  (equation 78).

859 Actually, in Takahashi et al. (2020, 2022) a fast 2D discrete circular convolution (Van Loan, 1992) is  
 860 used to process very large gravity and magnetic datasets efficiently. The convolutional equivalent layer  
 861 was applied to perform upward continuation of large magnetic datasets. Compared to the classical Fourier  
 862 approach, Takahashi et al.’s (2022) method produces smaller border effects without using any padding  
 863 scheme.

864 Without taking advantage of the symmetric BTTB structure of the sensitivity matrix (Takahashi et al.,  
 865 2020) that arises when gravimetric observations are measured on a horizontally regular grid, on a flat  
 866 surface and considering a regular grid of equivalent sources whithin a horizontal layer, Mendonça (2020)  
 867 explored the symmetry of the gravity kernel to reduce the number of forward model evaluations. By  
 868 exploting the symmetries of the gravity kernels and redundancies in the forward model evaluations on a  
 869 regular grid and combining the subspace solution based on eigenvectors of the gridded dataset, Mendonça  
 870 (2020) estimated the mass excess or deficiency produced by anomalous sources with positive or negative  
 871 density contrast.

## 872 6.2.8 The deconvolutional equivalent layer with BTTB matrices

873 To avoid the iterations of the conjugate gradient method in Takahashi et al. (2022), we can employ the  
 874 deconvolution process. Equation 81 shows that estimate the matrix  $\mathbf{V}$ , containing the elements of parameter  
 875 vector  $\mathbf{p}$ , is a inverse problem that could be solved by deconvolution. From equation 81, the matrix  $\mathbf{V}$  can  
 876 be obtain by deconvolution, i.e.

$$\mathbf{V} = \mathbf{F}_{2Q}^* \left[ \frac{(\mathbf{F}_{2Q} \mathbf{W} \mathbf{F}_{2P})}{\mathbf{L}} \right] \mathbf{F}_{2P}^*. \quad (82)$$

877 Equation 82 shows that the parameter vector (in matrix  $\mathbf{V}$ ) can be theoretically obtain by dividing each  
 878 potential-field observations (in matrix  $\mathbf{W}$ ) by each eigenvalues (in matrix  $\mathbf{L}$ ). Hence, the parameter vector  
 879 is constructed by element-by-element division of data by eigenvalues.

880 However, the deconvolution often is extremely unstable. This means that a small change in data can lead  
 881 to an enormous change in the estimated parameter. Hence, equation 82 requires regularization to be useful.

882 We used wiener deconvolution to obtain a stable solution, i.e.,

$$\mathbf{V} = \mathbf{F}_{2Q}^* \left[ (\mathbf{F}_{2Q} \mathbf{W} \mathbf{F}_{2P}) \frac{\mathbf{L}^*}{(\mathbf{L} \mathbf{L}^* + \mu)} \right] \mathbf{F}_{2P}^*, \quad (83)$$

883 where the matrix  $\mathbf{L}^*$  contains the complex conjugate eigenvalues and  $\mu$  is a parameter that controls the  
884 degree of stabilization.

### 885 6.3 Solution stability

886 The solution stability of the equivalent-layer methods is rarely addressed. Here, we follow the numerical  
887 stability analysis presented in Siqueira et al. (2017).

888 Let us assume noise-free potential-field data  $\mathbf{d}$ , we estimate a physical-property distribution  $\mathbf{p}$  (estimated  
889 solution) within the equivalent layer. Then, the noise-free data  $\mathbf{d}$  are contaminated with additive  $D$  different  
890 sequences of pseudorandom Gaussian noise, creating different noise-corrupted potential-field data  $\mathbf{d}_\ell^o$ ,  
891  $\ell = 1, \dots, D$ . From each  $\mathbf{d}_\ell^o$ , we estimate a physical-property distribution  $\hat{\mathbf{p}}_\ell$  within the equivalent layer.

892 Next, for each noise-corrupted data  $\mathbf{d}_\ell^o$  and estimated solution  $\hat{\mathbf{p}}_\ell$ , the  $\ell$ th model perturbation  $\delta p_\ell$  and the  
893  $\ell$ th data perturbation  $\delta d_\ell$  are, respectively, evaluated by

$$\delta p_\ell = \frac{\|\hat{\mathbf{p}}_\ell - \mathbf{p}\|_2}{\|\mathbf{p}\|_2}, \quad \ell = 1, \dots, D, \quad (84)$$

894 and

$$\delta d_\ell = \frac{\|\mathbf{d}_\ell^o - \mathbf{d}\|_2}{\|\mathbf{d}\|_2}, \quad \ell = 1, \dots, D. \quad (85)$$

895 Regardless of the particular method used, the following inequality (Aster et al., 2018, p. 66) is applicable:

$$\delta p_\ell \leq \kappa \delta d_\ell, \quad \ell = 1, \dots, D, \quad (86)$$

896 where  $\kappa$  is the constant of proportionality between the model perturbation  $\delta p_\ell$  (equation 84) and the data  
897 perturbation  $\delta d_\ell$  (equation 85). The constant  $\kappa$  acts as the condition number of an invertible matrix in a  
898 given inversion, and thus measures the instability of the solution. The larger (smaller) the value of  $\kappa$  the  
899 more unstable (stable) is the estimated solution.

900 Equation 86 shows a linear relationship between the model perturbation and the data perturbation. By  
901 plotting  $\delta p_\ell$  (equation 84) against  $\delta d_\ell$  (equation 85) produced by a set of  $D$  estimated solution obtained by  
902 applying a given equivalent-layer method, we obtain a straight line behaviour described by equation 86.  
903 By applying a linear regression, we obtain a fitted straight line whose estimated slope ( $\kappa$  in equation 86)  
904 quantifies the solution stability.

905 Here, the analysis of solution stability is numerically conducted by applying the classical equivalent-  
906 layer technique with zeroth-order Tikhonov regularization, the convolutional method for gravimetric and  
907 magnetic data, the deconvolutional method (equation 82) and the deconvolutional method with different  
908 values for the Wiener stabilization (equation 83).

## 7 NUMERICAL SIMULATIONS

### 909 7.1 Floating-point operations calculation

910 To measure the computational effort of the different algorithms to solve the equivalent layer linear system,  
 911 a non-hardware dependent method can be useful because allow us to do direct comparison between them.  
 912 Counting the floating-point operations (*flops*), i.e., additions, subtractions, multiplications and divisions is  
 913 a good way to quantify the amount of work of a given algorithm (Golub and Loan, 2013). For example, the  
 914 number of *flops* necessary to multiply two vectors  $\mathbb{R}^D$  is  $2D$ . A common matrix-vector multiplication with  
 915 dimension  $\mathbb{R}^{D \times D}$  and  $\mathbb{R}^D$ , respectively, is  $2D^2$  and a multiplication of two matrices  $\mathbb{R}^{D \times D}$  is  $2D^3$ . Figure  
 916 1 shows the total flops count for the different methods presented in this review with a crescent number of  
 917 data, ranging from 10,000 to 1,000,000.

#### 918 7.1.1 Normal equations using Cholesky decomposition

919 The equivalent sources can be estimated directly from solving the normal equations 18. In this work  
 920 we will use the Cholesky decompositions method to calculate the necessary *flops* for a overdetermined  
 921 problem (equation 20). In this method it is necessary to calculate the lower triangule matrix of the left side  
 922 equation ( $1/2D^3$ ), the Cholesky factor ( $1/3D^3$ ), a matrix-vector multiplication ( $2D^2$ ) and finally solving  
 923 the triangular system ( $2D^2$ ), totalizing

$$f_{classical} = \frac{5}{6}D^3 + 4D^2 \quad (87)$$

#### 924 7.1.2 Window method (Leão and Silva, 1989)

925 The moving data-window scheme (Leão and Silva, 1989) solve  $M$  linear systems with much smaller  
 926 sizes (equation 60b) in comparison to the original  $D \times D$  system. For our results we are considering a  
 927 data-window of the same size of wich the authors presented in theirs work ( $D' = 49$ ) and the same number  
 928 of equivalent sources ( $P' = 225$ ). Using the algorithm 1 as a guide, we have a matrix-matrix multiplication  
 929 ( $2D'^2P'$ ), a scalar multiplication and a sum with diagonal matrices ( $D'$  each), a matrix inverse ( $D'^3$ ),  
 930 another matrix-matrix product ( $2D'P'^2$ ), a matrix-vetor product ( $2P'D'$ ) and finally a iteration with a  
 931 vector-vector multiplication ( $2D'$ ). The *flops* are

$$f_{window} = M2D' + 2P'D' + \frac{2D'^3}{3} + 2D' + 2D'P'(D' + P') \quad (88)$$

932 Here we are considering a  $2D'^3/3$  *flops* count for the Gauss-Jordan inverse matrix algorithm and  $M = D$   
 933 as we want to calculate the same number of transformations as observation points. Notice that this algorithm  
 934 takes advantage of a regular grid to calculate only once the inverse matrix and the harmonic functions of  
 935  $a'$ , with a irregular grid these calculations would be necessary at each iteration. Also this method does  
 936 not store the equivalent sources estimatives saving computer memory, however, any other potential field  
 937 transformation would require to run the algorithm again with the compatible harmonic function  $a'$  (equation  
 938 5).

#### 939 7.1.3 PEL method (Oliveira Jr. et al., 2013)

940 The polynomial equivalent layer uses a similiar approach of moving windows from Leão and Silva (1989).  
 941 For this operations calculation (equation 32) we used a first degree polynomial (two variables) and each

942 window contains  $D' = 1,000$  observed data and  $P' = 1,000$  equivalent sources. Following the steps given  
 943 in (Oliveira Jr. et al., 2013) the total *flops* becomes

$$f_{pel} = \frac{1}{3}N_c^3 + 2N_c^2 + 2DP'N_c + N_c^2D + 2N_cD + 2DC \quad (89)$$

944 where  $N_c$  is the number of constant coefficients for the first degree polynomial ( $C = 3$ ) times the number  
 945 of windows ( $C \times M$ ).

#### 946 7.1.4 Conjugate gradient least square (CGLS)

947 The CGLS method is a very stable and fast algorithm for solving linear systems iteratively. Its computa-  
 948 tional complexity envolves a matrix-vector product outside the loop ( $2D^2$ ), two matrix-vector products  
 949 inside the loop ( $4D^2$ ) and six vector products inside the loop ( $12D$ ) (Aster et al., 2018)

$$f_{ccls} = 2D^2 + it(4D^2 + 12D) \quad (90)$$

#### 950 7.1.5 Wavelet compression method with CGLS (Li and Oldenburg, 2010)

951 For the wavelet method (equation 63) we have calculated a compression rate of 98% ( $C_r = 0.02$ )  
 952 as the authors used in Li and Oldenburg (2010) and the wavelet transformation requiring  $\log_2(D)$  *flops*  
 953 each (equations 34 and 35), with its inverse also using the same number of operations (equation 38). The  
 954 normalization using diagonal matrix  $\mathbf{L}$  in equations 36, 37 and 38 can be simplified to a matrix-vector  
 955 product ( $2DP$ ) and two vector-vector products( $2P_{each}$ ). Combined with the conjugate gradient least  
 956 square necessary steps and iterations, the number of *flops* are

$$f_{wavelet} = 2DP + 4P + 2DC_r + 4D\log_2(D) + it(4D\log_2(D) + 4DC_r + 12C_r) \quad (91)$$

#### 957 7.1.6 Fast equivalent layer for gravity data (Siqueira et al., 2017)

958 The fast equivalent layer from Siqueira et al. (2017) solves the linear system in *it* iterations. The main  
 959 cost of this method (algorithm 5) is the matrix-vector multiplication to assess the predicted data ( $2D^2$ ) and  
 960 three simply element by element vector sum, subtraction and division ( $3D$  total)

$$f_{siqueira} = it(3D + 2D^2) \quad (92)$$

#### 961 7.1.7 Convolutional equivalent layer for gravity data (Takahashi et al., 2020)

962 This methods replaces the matrix-vector multiplication of the iterative fast-equivalent technique (Siqueira  
 963 et al., 2017) by three steps, involving a Fourier transform, an inverse Fourier transform, and a Hadamard  
 964 product of matrices (equation 53). Considering that the first column of our BCCB matrix has  $4D$  elements,  
 965 the flops count of this method is a combination of algorithms 5 and 7

$$f_{convgrav} = \kappa 4D \log_2(4D) + it(27D + \kappa 8D \log_2(4D)) \quad (93)$$

966 In the resultant count we considered a radix-2 algorithm for the fast Fourier transform and its inverse,  
 967 which has a  $\kappa$  equals to 5 and requires  $\kappa 4D \log_2(4D)$  flops each. The Hadarmard product of two matrices  
 968 of  $4D$  elements with complex numbers takes  $24D$  flops. Note that equation 93 is different from the one

969 presented in Takahashi et al. (2020) because we also added the flops necessary to calculate the eigenvalues  
 970 in this form. It does not differentiate much in order of magnitude because the iterative part is the most  
 971 costful.

### 972 7.1.8 Convolutional equivalent layer for magnetic data (Takahashi et al., 2022)

973 The convolutional equivalent layer for magnetic (algorithm 6) data uses the same flops count of the main  
 974 operations as in the gravimetric case (equation 53), the difference is the use of the conjugate gradient  
 975 algorithm to solve the inverse problem. It requires a Hadamard product outside of the iterative loop and the  
 976 matrix-vector and vector-vector multiplications inside the loop as seem in equation 90.

$$f_{convmag} = \kappa 16D \log_2(4D) + 24D + it(\kappa 16D \log_2(4D) + 60D) \quad (94)$$

### 977 7.1.9 Deconvolutional method

978 The deconvolution method does not require an iterative algorithm, rather it solves the estimative of the  
 979 physical properties in a single step using the  $4D$  eigenvalues of the BCCB matrix as in the convolutional  
 980 method. From equation 82 it is possible to deduce this method requires two fast Fourier transform  
 981 ( $\kappa 4D \log_2(4D)$ ), one for the eigenvalues and another for the data transformation, an element by element  
 982 division ( $24D$ ) and finally, a fast inverse Fourier transform for the final estimative ( $\kappa 4D \log_2(4D)$ ).

$$f_{deconv} = \kappa 12D \log_2(4D) + 24D \quad (95)$$

983 Using the deconvolutional method with a Wiener stabilization adds two multiplications of complex  
 984 elements of the conjugates eigenvalues ( $24D$  each) and the sum of  $4D$  elements with the stabilization  
 985 parameter  $\mu$  as shown in equation 83

$$f_{deconvwiener} = \kappa 12D \log_2(4D) + 76D \quad (96)$$

## 8 SYNTHETIC DATA SIMULATIONS

For all applications, we generate a model composed by two spheres and a polygonal prism in a regular spaced grid of  $50 \times 50$ . The upper left sphere has a density contrast of  $600 \text{ kg/m}^3$ , the right upper sphere a negative contrast of  $-500 \text{ kg/m}^3$  and the bottom prism is equal to  $550 \text{ kg/m}^3$ . To generate the magnetic data, the bodies are in the same position and all of them have the same magnetization intensity and direction ( $3.46 \text{ A/m}$  intensity,  $35.26^\circ$  inclination and  $45.0^\circ$  declination) within a simulated geomagnetic field direction of  $20.0^\circ$  inclination and  $35.0^\circ$  declination. These synthetic datas are shown in figures 3 and 7, respectively.

### 8.1 Stability analysis

For the stability analysis we show the comparison of the normal equations solution (equation 59) with zeroth-order Tikhonov regularization (Aster et al., 2018), the convolutional method (equation 81), the deconvolutional method (equation 82) and the deconvolutional method with different values for the Wiener stabilization (equation 83). We create 21 data sets, for both gravity and magnetic data, adding a crescent pseudo-random noise to the original data, which varies from 0% to 10% of the maximum anomaly value in intervals of 0.5%. These noises has mean equal to zero and a Gaussian distribution. These synthetic datas are shown in figures 3 and 7, where panel (A) of each figure represents the noise free data and panel (B) is the maximum noised data for gravity and magnetic, respectively.

Figure 2 shows how the euclidian norm of the equivalent sources residuals varies as the level of the noise is increased for the gravimetric data. We can see that for all methods, a linear tendency can be observed as it is expected. The inclination of the straight line is a indicative of the stability of each method. As show in the graph the deconvolutional method is very unstable and it is really necessary to use a stabilization method to have a good parameter estimative. In contrast, a correct value of the stabilization parameter is necessary to not overshoot the smoothness of the solution as it is the case for the zeroth-order Tikhonov regularization as well. Using this gravimetric data, the optimal value for the Wiener stabilization parameter is  $\mu = 10^{-20}$ .

Figure 4 shows the comparison of the predicted data for each method with the original data (figure 3) using the most noised-corrupted data from the set of the stability analysis. The classical with zeroth-order Tikhonov regularization and the convolutional methods (figures 4(A) and 4(B)) yield very similar results for the predicted data confirming its similarities with the stabilization despite the bid difference in floating-point operations. Figure 4(C) shows the deconvolutional method without a stabilization and demonstrates the necessity to use it for this method. Figure 4(D) shows the deconvolutional method with Wiener stabilization  $\mu = 10^{-15}$  which is too high, demonstrating the over smoothness of the predicted data. Figures 4(E) and 4(F) shows the predicted data for an optimal value of the Wiener parameter  $\mu = 10^{-20}$  and a low value  $\mu = 10^{-25}$ , respectively.

The upward continuation is a processing technique to visualize the data in a higher altitude. In practice is expected a lower amplitude signal and a smoother data as the high frequency anomalies tends to disappear. Figure 5(A) shows the true modeled upward data at an height of  $-500 \text{ m}$ . Figures 5(B), (C), (D) and (E) show the result of the upward processing for the classical, convolutional, deconvolutional and the deconvolutional with Wiener parameter  $\mu = 10^{-20}$ , respectively. It is clear that all methods seems to predict the upward data very reasonable, except the deconvolutional method without stabilization.

For the magnetic data, figure 6 shows a very similar behavior of the stability as the previous case. The Wiener parameter seems to have the best solution for  $\mu = 10^{-13}$ . For both types of data the best Wiener

1027 parameter seems to be one that produces a low slope for the straight line in the stability analysis, discordant  
1028 from the classical and convolutional methods.

1029 Figure 8 shows the comparison of the predicted data for each method with the original magnetic data in  
1030 figure 7 using the most noised-corrupted data modeled from the stability analysis. As the previous case the  
1031 classical (figure 8(A)) and the convolutional (figure 8(B)) methods have very similar predicted data but  
1032 estimated with less orders of magnitude in floating-point operations. The deconvolutional (figure 8(C)) have  
1033 have a strong disagreement with the observed data showing the need for a stabilization method. Figure  
1034 8(D) has a value of  $\mu = 10^{-10}$  and the predicted data became to smooth by it. The optimal value of the  
1035 Wiener parameter is shown in figure 8(E) with  $\mu = 10^{-13}$  and figure 8(F) shows a predicted data with a  
1036 low stabilization value with  $\mu = 10^{-16}$ .

1037 Figure 9(A) shows the true modeled upward data at an height of  $-1400$  m. Figures 9(B), (C), (D) and  
1038 (E) show the result of the upward processing for the classical, convolutional, deconvolutional and the  
1039 deconvolutional with Wiener parameter  $\mu = 10^{-13}$ , respectively. As in the gravimetric case, all methods  
1040 seems to predict the upward data, except the deconvolutional method without stabilization.

## 9 REAL DATA RESULTS

1041 In this section, we show the applications of the convolutional and the deconvolutional strategies in a real  
1042 data set from the North of Brazil. The region is located in the Carajás Mineral Province (CMP) in the  
1043 Amazon craton (Moroni et al., 2001; Villas and Santos, 2001). This area is known for its intensive mineral  
1044 exploration such as iron, copper, gold, manganese, and, recently, bauxite.

1045 **9.1 Geological setting**

1046 The Amazon craton is one of the largest and least-known Archean-Proterozoic areas in the world,  
1047 comprehending a region with a thousand square kilometers. It is one of the main tectonic units in South  
1048 America, which is covered by five Phanerozoic basins: Maranhão (Northeast), Amazon (Central), Xingu-  
1049 Alto Tapajós (South), Parecis (Southwest), and Solimões (West). The craton is limited by the Andean  
1050 Orogenic Belt to the west and the by Araguaia Fold Belt to the east and southeast. The Amazon craton has  
1051 been subdivided into provinces according to two models, one geochronological and the other geophysical-  
1052 structural (Amaral, 1974; Teixeira et al., 1989; Tassinari and Macambira, 1999). Thus, seven geological  
1053 provinces with distinctive ages, evolution, and structural patterns can be observed, namely : (i) Carajás with  
1054 two domains - the Mesoarchean Rio Maria and Neoarchean Carajás; (ii) Archean-Paleoproterozoic Central  
1055 Amazon, with Iriri-Xingu and Curuá-Mapuera domains; (ii) Trans-Amazonian (Ryacian), with the Amapá  
1056 and Bacajá domains; (iv) the Orosinian Tapajós-Parima, with Peixoto de Azevedo, Tapajós, Uaimiri, and  
1057 Parima domains; (v) Rondônia-Juruena (Statherian), with Jamari, Juruena, and Jauru domains; (vi) The  
1058 Statherian Rio Negro, with Rio Negro and Imeri domains; and (vii) Sunsás (Meso-Neoproterozoic), with  
1059 Santa Helena and Nova Brasilândia domains (Santos et al., 2000). Nevertheless, we focus this work only  
1060 on the Carajás Province.

1061 The Carajás Mineral Province (CMP) is located in the east-southeast region of the craton, within an old  
1062 tectonically stable nucleus in the South American Plate that became tectonically stable at the beginning of  
1063 Neoproterozoic (Salomao et al., 2019). This area has been the target of intensive exploration at least since  
1064 the final of the '60s, after the discovery of large iron ore deposits. There are several greenstone belts in the  
1065 region, among them are the Andorinhas, Inajá, Cumaru, Carajás, Serra Leste, Serra Pelada, and Sapucaia  
1066 (Santos et al., 2000). The mineralogic and petrologic studies in granite stocks show a variety of minerals  
1067 found in the province, such as amphibole, plagioclase, biotite, ilmenite, and magnetite (Cunha et al., 2016).  
1068 These two latter minerals contribute to the high magnetic response in the CMP area. This fact opens the  
1069 opportunity for potential field applications for the geophysical description of the area.

1070 **9.2 Potential field data applications**

1071 Here we compare the performance of the convolutional and deconvolutional algorithms in a real potential  
1072 field data set. We focus the application on a region in the Southeast of the State of Pará. The aeromagnetic  
1073 data were acquired by the Geological Survey of Brazil-CPRM. The survey area covers  $\approx 58000 \text{ km}^2$  with  
1074 high-resolution gravity and magnetic data. The flight and the tie lines were acquired and spaced at  $3 \text{ km}$   
1075 and  $12 \text{ km}$  oriented in the directions  $N - S$  and  $E - W$ , respectively, with a mean flight height of  $900 \text{ m}$   
1076 above the ground. For both applications, we interpolated gravity and magnetic anomalies data, calculating  
1077 the data set in a grid of  $1000 \times 500$  ( $N = 500000$  observation points) at the same mean flight height. About  
1078 the computational resources, we processed both data on an Intel Core i7 7700HQ@2.8 GHz processor and  
1079 16GB RAM. We show in Figure 10 and Figure 12 the interpolated aerogravimetric and aeromagnetic data,  
1080 respectively. We also use the same equivalent layer grid configuration in gravity and magnetic applications.

1081 This setup is composed by a grid of  $1000 \times 500$  equivalent sources (a total number of  $M = 500000$  points)  
1082 positioned below the observation plane, but a different depth in each application.

1083 We apply both strategies to the gravimetric case. We set a depth for the equivalent layer equal to  $1200\text{ m}$   
1084 below the observation plane. Figure 11A and Figure 11C show the predicted data for convolutional and  
1085 deconvolutional strategies. The residual maps (the difference between the observed and predicted data)  
1086 are show in figures 11B and 11D for the convolutional and deconvolutional equivalent-layer technique,  
1087 respectively. For the convolutional case, the mean residual and standard deviation values are  $\approx 0.00\text{ mGal}$   
1088 and  $\approx 0.15\text{ mGal}$ , respectively. For the deconvolutional case, the mean residual and standard deviation  
1089 values are  $\approx 0.46\text{ mGal}$  and  $\approx 1.23\text{ mGal}$ , respectively. These last results show that the estimated density  
1090 distributions (not shown) fit the observed data for both applications. To show the performance of the  
1091 algorithms, we performed an upward continuation by using the estimated density distributions (figures 11E  
1092 and 11F). There is a little difference on the processing time between both strategies. The convolutional  
1093 algorithm took  $\approx 9.18\text{ s}$  and the deconvolutional algorithm took  $\approx 0.53\text{ s}$ . We conclude that both strategies  
1094 are capable of processing gravimetric observations from large areas with dense coverage data. Despite a  
1095 little difference in processing time, the deconvolutional equivalent-layer technique proved to be faster than  
1096 the convolutional strategy.

1097 Finally, we test the convolutional and deconvolutional algorithms for processing total-field anomalies.  
1098 We stress that the Carajás area is very large and the main field direction varies significantly. For this reason,  
1099 we consider a mean direction for the main field equal to  $-19.865^\circ$  and  $-7.43915^\circ$  (the same as the mid  
1100 location of the area) for the inclination and declination, respectively. Furthermore, we are not considering  
1101 the knowledge about the magnetization direction of the sources, and choose a magnetization direction for  
1102 the equivalent layer equal to the main field direction. For this application, we set a depth of  $900\text{ m}$  (below  
1103 the observation plane) for the equivalent layer. Figure 12A and Figure 12C show the predicted data for  
1104 convolutional and deconvolutional algorithms. The residual maps (the difference between the observed and  
1105 predicted data) are show in figures 12B and 12D for the convolutional and deconvolutional techniques,  
1106 respectively. The convolutional equivalent layer produced a mean residual and standard deviation values  
1107 of  $\approx 0.06\text{ nT}$  and  $\approx 1.97\text{ nT}$ , respectively. The deconvolutional algorithm produced a mean residual  
1108 and standard deviation values of  $\approx 18.99\text{ nT}$  and  $\approx 33.64\text{ nT}$ , respectively. To show the performance  
1109 of the algorithms, we performed an upward continuation (figures 12E and 12F) by using the estimated  
1110 magnetic-moment distributions (not shown). Similarly to the gravity application, the deconvolutional  
1111 equivalent layer presents faster results than the convolutional algorithm. The deconvolutional and the  
1112 convolutional approaches took  $\approx 0.89\text{ s}$  and  $\approx 82.08\text{ s}$ , respectively. Despite the difference between the  
1113 processing time of both strategies and considering the mean value of residuals and standard deviations, we  
1114 conclude that the convolutional strategy fits the observation data better than the deconvolutional approach.

## 10 DISCUSSION AND CONCLUSION

1115 We show in this work that the computational cost of the equivalent layer can vary from up to  $10^9$  flops  
1116 depending on the method without compromising the linear system stability. The convolutional method has  
1117 the necessity of using a regular grid, a problem that can be easily overcome with a gridding or interpolation  
1118 method. The deconvolution is one of the fastest method but, has two drawbacks besides the regular grid,  
1119 the necessity of choosing the correct parameter of stabilization and also a higher residual and border effects  
1120 after processing, that can be seen from the upward continuation of the real data from Carajás. The authors  
1121 advise cautionary use of the latter method despite the computational cost reduction.

## CONFLICT OF INTEREST STATEMENT

1122 The authors declare that the research was conducted in the absence of any commercial or financial  
1123 relationships that could be construed as a potential conflict of interest.

## AUTHOR CONTRIBUTIONS

1124 The Author Contributions section is mandatory for all articles, including articles by sole authors. If an  
1125 appropriate statement is not provided on submission, a standard one will be inserted during the production  
1126 process. The Author Contributions statement must describe the contributions of individual authors referred  
1127 to by their initials and, in doing so, all authors agree to be accountable for the content of the work. Please  
1128 see here for full authorship criteria.

## FUNDING

1129 Diego Takahashi was supported by a Post-doctoral scholarship from CNPq (grant 300809/2022-0) Valéria  
1130 C.F. Barbosa was supported by fellowships from CNPq (grant 309624/2021-5) and FAPERJ (grant  
1131 26/202.582/2019). Vanderlei C. Oliveira Jr. was supported by fellowships from CNPq (grant 315768/2020-  
1132 7) and FAPERJ (grant E-26/202.729/2018).

## ACKNOWLEDGMENTS

1133 We thank the Brazilian federal agencies CAPES, CNPq, state agency FAPERJ and Observatório Nacional  
1134 research institute and Universidade do Estado do Rio de Janeiro.

## DATA AVAILABILITY STATEMENT

1135 The datasets generated for this study can be found in the frontiers-paper Github repository link:  
1136 <https://github.com/DiegoTaka/frontiers-paper>.

## REFERENCES

- 1137 Amaral, G. (1974). *Geologia Pré-Cambriana da Região Amazônica*. Ph.D. thesis, Universidade de São  
1138 Paulo
- 1139 Aster, R. C., Borchers, B., and Thurber, C. H. (2018). *Parameter estimation and inverse problems*  
1140 (Elsevier)
- 1141 Barbosa, V. C. F., Silva, J. B., and Medeiros, W. E. (1997). Gravity inversion of basement relief using  
1142 approximate equality constraints on depths. *Geophysics* 62, 1745–1757
- 1143 Barnes, G. and Lumley, J. (2011). Processing gravity gradient data. *Geophysics* 76, I33–I47. doi:10.1190/  
1144 1.3548548
- 1145 Cordell, L. (1992). A scattered equivalent-source method for interpolation and gridding of potential-field  
1146 data in three dimensions. *Geophysics* 57, 629–636
- 1147 Cunha, I. R., Dall’Agnol, R., and Feio, G. R. L. (2016). Mineral chemistry and magnetic petrology of the  
1148 archean planalto suite, carajás province – amazonian craton: Implications for the evolution of ferroan  
1149 archean granites. *Journal of South American Earth Sciences* 67, 100–121
- 1150 Dampney, C. N. G. (1969). The equivalent source technique. *Geophysics* 34, 39–53. doi:10.1190/1.  
1151 1439996

- 1152 Davis, K. and Li, Y. (2011). Fast solution of geophysical inversion using adaptive mesh, space-filling  
1153 curves and wavelet compression. *Geophysical Journal International* 185, 157–166. doi:10.1111/j.  
1154 1365-246X.2011.04929.x
- 1155 Davis, P. J. (1979). *Circulant matrices* (John Wiley & Sons, Inc.)
- 1156 Friedman, J. H. (2001). Greedy function approximation: a gradient boosting machine. *Annals of statistics* ,  
1157 1189–1232
- 1158 Friedman, J. H. (2002). Stochastic gradient boosting. *Computational statistics and data analysis* 38,  
1159 367–378
- 1160 Golub, G. H. and Loan, C. F. V. (2013). *Matrix Computations (Johns Hopkins Studies in the Mathematical  
1161 Sciences)* (Johns Hopkins University Press), 4 edn.
- 1162 Guspí, F. and Novara, I. (2009). Reduction to the pole and transformations of scattered magnetic data using  
1163 newtonian equivalent sources. *Geophysics* 74, L67–L73
- 1164 Horn, R. A. and Johnson, C. R. (1991). *Topics in Matrix Analysis* (Cambridge University Press), 1 edn.
- 1165 Jirigalatu, J. and Ebbing (2019). A fast equivalent source method for airborne gravity gradient data.  
1166 *Geophysics* 84, G75–G82. doi:10.1190/GEO2018-0366.1
- 1167 Kellogg, O. D. (1929). *Foundations of Potential Theory* (Frederick Ungar Publishing Company)
- 1168 Kennett, B., Sambridge, M., and Williamson, P. (1988). Subspace methods for large inverse problems with  
1169 multiple parameter classes. *Geophysical Journal International* 94, 237–247
- 1170 Leão, J. W. D. and Silva, J. B. C. (1989). Discrete linear transformations of potential field data. *Geophysics*  
1171 54, 497–507. doi:10.1190/1.1442676
- 1172 Li, Y. and Oldenburg, D. W. (2010). Rapid construction of equivalent sources using wavelets. *Geophysics*  
1173 75, L51–L59. doi:10.1190/1.3378764
- 1174 Mendonça, C. A. (2020). Subspace method for solving large-scale equivalent layer and density mapping  
1175 problems. *Geophysics* 85, G57–G68. doi:10.1190/geo2019-0302.1
- 1176 Mendonça, C. A. and Silva, J. B. C. (1994). The equivalent data concept applied to the interpolation of  
1177 potential field data. *Geophysics* 59, 722–732. doi:10.1190/1.1443630
- 1178 Moroni, M., Girardi, V., and Ferrario, A. (2001). The serra pelada au-pge deposit, serra dos carajás (pará  
1179 state, brazil): geological and geochemical indications for a composite mineralising process. *Mineralium  
1180 Deposita* 36, 768–785
- 1181 Neudecker, H. (1969). Some theorems on matrix differentiation with special reference to kronecker matrix  
1182 products. *Journal of the American Statistical Association* 64, 953–963. doi:10.1080/01621459.1969.  
1183 10501027
- 1184 Oldenburg, D., McGillivray, P., and Ellis, R. (1993). Generalized subspace methods for large-scale inverse  
1185 problems. *Geophysical Journal International* 114, 12–20
- 1186 Oliveira Jr., V. C., Barbosa, V. C. F., and Uieda, L. (2013). Polynomial equivalent layer. *Geophysics* 78,  
1187 G1–G13. doi:10.1190/geo2012-0196.1
- 1188 Salomao, G. N., Dall’Agnol, R., Angelica, R. S., Figueiredo, M. A., Sahoo, P. K., Medeiros-filho, C. A.,  
1189 et al. (2019). Geochemical mapping and estimation of background concentrations in soils of carajás  
1190 mineral province, eastern amazonian craton, brazil. *Geochemistry: Exploration, Environment, Analysis*  
1191 19, 431–447
- 1192 Santos, J. O. S., Hartmann, L. A., Gaudette, H. E., Groves, D. I., Mcnaughton, M. J., and Fletcher, I. R.  
1193 (2000). A new understanding of the provinces of the amazon craton based on integration of field mapping  
1194 and u-pb and sm-nd geochronology. *Gondwana Research* 3, 453–488
- 1195 Siqueira, F. C., Oliveira Jr, V. C., and Barbosa, V. C. (2017). Fast iterative equivalent-layer technique for  
1196 gravity data processing: A method grounded on excess mass constraint. *Geophysics* 82, G57–G69

- 1197 Skilling, J. and Bryan, R. (1984). Maximum entropy image reconstruction-general algorithm. *Monthly*  
1198   *Notices of the Royal Astronomical Society*, Vol. 211, NO. 1, P. 111, 1984 211, 111
- 1199 Soler, S. R. and Uieda, L. (2021). Gradient-boosted equivalent sources. *Geophysical Journal International*  
1200   227, 1768–1783. doi:10.1093/gji/ggab297
- 1201 Takahashi, D., Oliveira, V. C., and Barbosa, V. C. (2022). Convolutional equivalent layer for magnetic data  
1202   processing. *Geophysics* 87, 1–59
- 1203 Takahashi, D., Oliveira Jr, V. C., and Barbosa, V. C. (2020). Convolutional equivalent layer for gravity data  
1204   processing. *Geophysics* 85, G129–G141
- 1205 Tassinari, C. C. and Macambira, M. J. (1999). Geochronological provinces of the amazonian craton.  
1206   *Episodes* 22, 174–182
- 1207 Teixeira, W., Tassinari, C., Cordani, U. G., and Kawashita, K. (1989). A review of the geochronology of  
1208   the amazonian craton: Tectonic implications. *Precambrian Research* 42, 213–227
- 1209 Van Loan, C. (1992). *Computational Frameworks for the Fast Fourier Transform* (SIAM)
- 1210 Villas, R. N. and Santos, M. (2001). Gold deposits of the carajás mineral province: deposit types and  
1211   metallogenesis. *Mineralium Deposita* 36, 300–331
- 1212 Xia, J. and Sprowl, D. R. (1991). Correction of topographic distortion in gravity data. *Geophysics* 56,  
1213   537–541
- 1214 Xia, J., Sprowl, D. R., and Adkins-Heljeson, D. (1993). Correction of topographic distortions in potential-  
1215   field data; a fast and accurate approach. *Geophysics* 58, 515–523. doi:10.1190/1.1443434

## 11 SUPPLEMENTARY TABLES AND FIGURES

### 1216 11.1 Figures

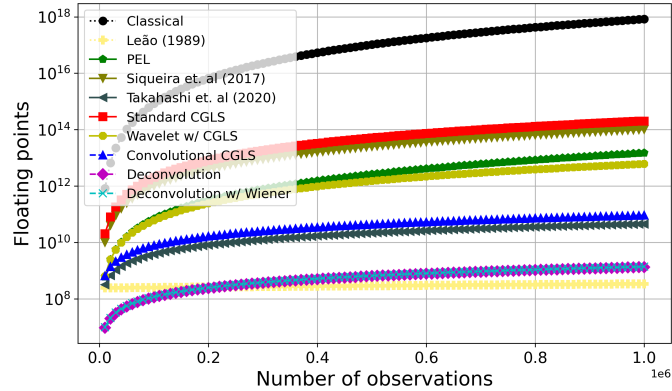


**Figure 1.** Number of *flops* for many of the methods described in this work to estimate the equivalent sources using gravity data. The range of observations varies from 10,000 to 1,000,000.

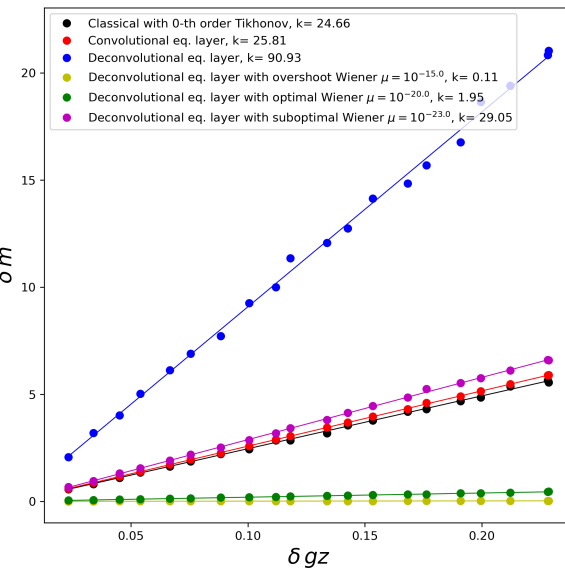


**Figure 2.** Stability analysis of some of the equivalent layer methods of the gravimetric case.

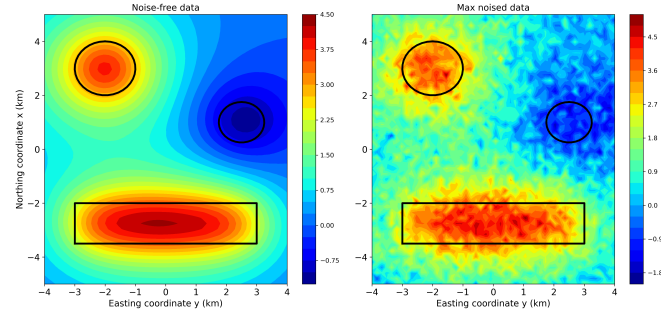


**Figure 3.** Synthetic data of the gravimetric case. The observations points are placed in a regular grid of  $50 \times 50$ . Panel (A) shows the noise-free data and panel (B) shows the maximum noised data (10%).

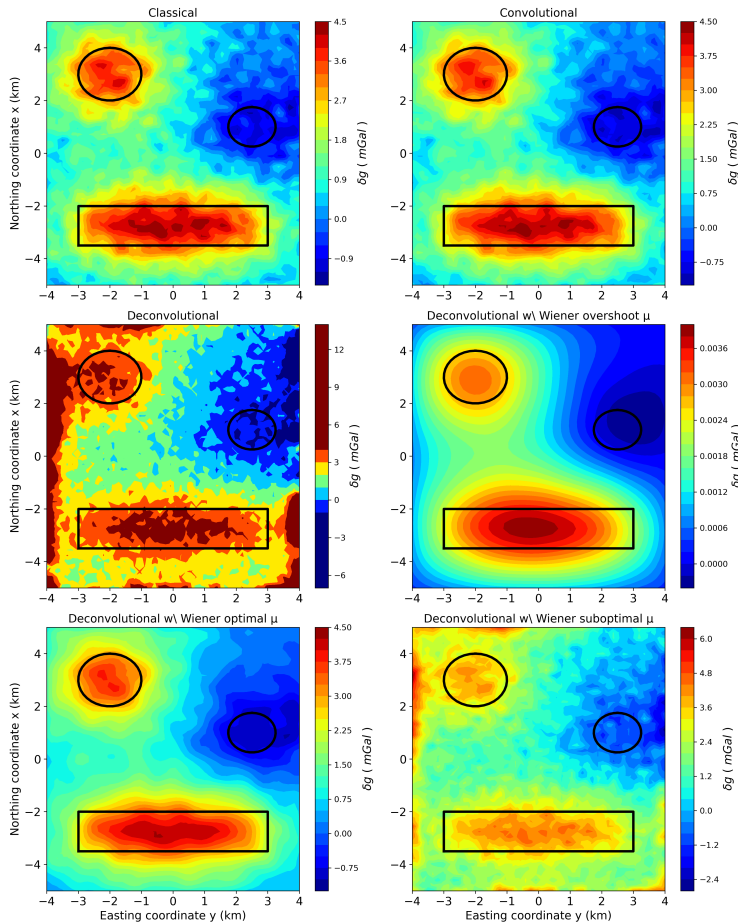


**Figure 4.** Predicted gravity data for different methods of the equivalent layer with maximum level of noise. Panel (A) is the classical method, (B) is the convolutional, (C) is the deconvolutional, (D) is the deconvolutional method using Wiener stabilization with a too high value for  $\mu$ , (E) is the deconvolutional method using Wiener stabilization with an optimal value for  $\mu$  and (F) is the deconvolutional method using Wiener stabilization with a too low value for  $\mu$ .

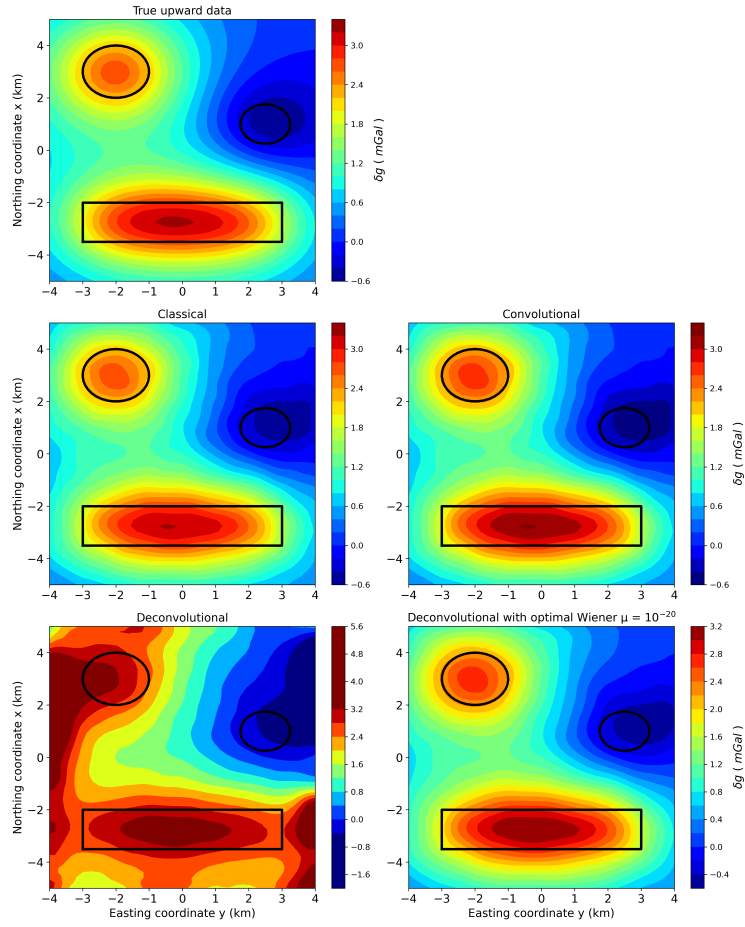


**Figure 5.** True noiseless upward gravimetric data at  $z_i = -500$  m height and predicted data for different methods of the equivalent layer with maximum level of noise. Panel **(A)** is the true upward gravity data, Panel **(B)** is the classical method, **(C)** is the convolutional, **(D)** is the deconvolutional, **(E)** is the deconvolutional method using Wiener stabilization with a optimal value for  $\mu = 10^{-20}$ .

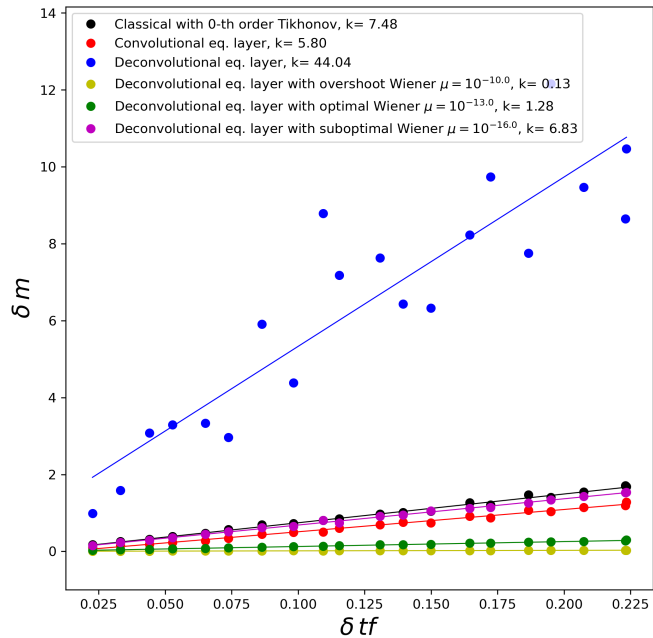


**Figure 6.** Stability analysis of some of the equivalent layer methods of the magnetic case.

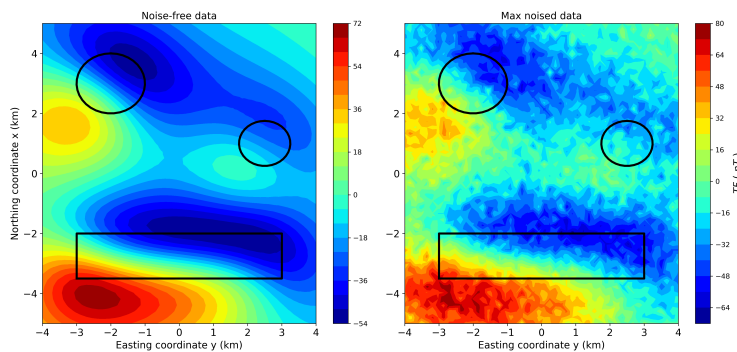


**Figure 7.** Synthetic data of the magnetic case. The observations points are placed in a regular grid of  $50 \times 50$ . Panel (A) shows the noise-free data and panel (B) shows the maximum noised data (10%).

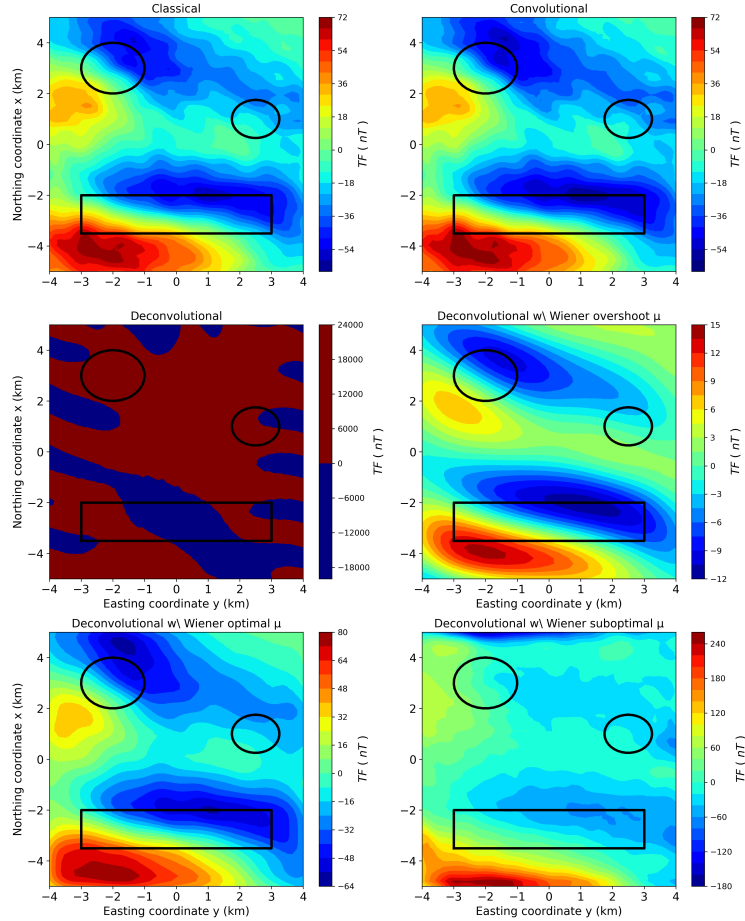


**Figure 8.** Predicted magnetic data for different methods of the equivalent layer with maximum level of noise. Panel **(A)** is the classical method, **(B)** is the convolutional, **(C)** is the deconvolutional, **(D)** is the deconvolutional method using Wiener stabilization with a too high value for  $\mu$ , **(E)** is the deconvolutional method using Wiener stabilization with a optimal value for  $\mu$  and **(F)** is the deconvolutional method using Wiener stabilization with a too low value for  $\mu$ .

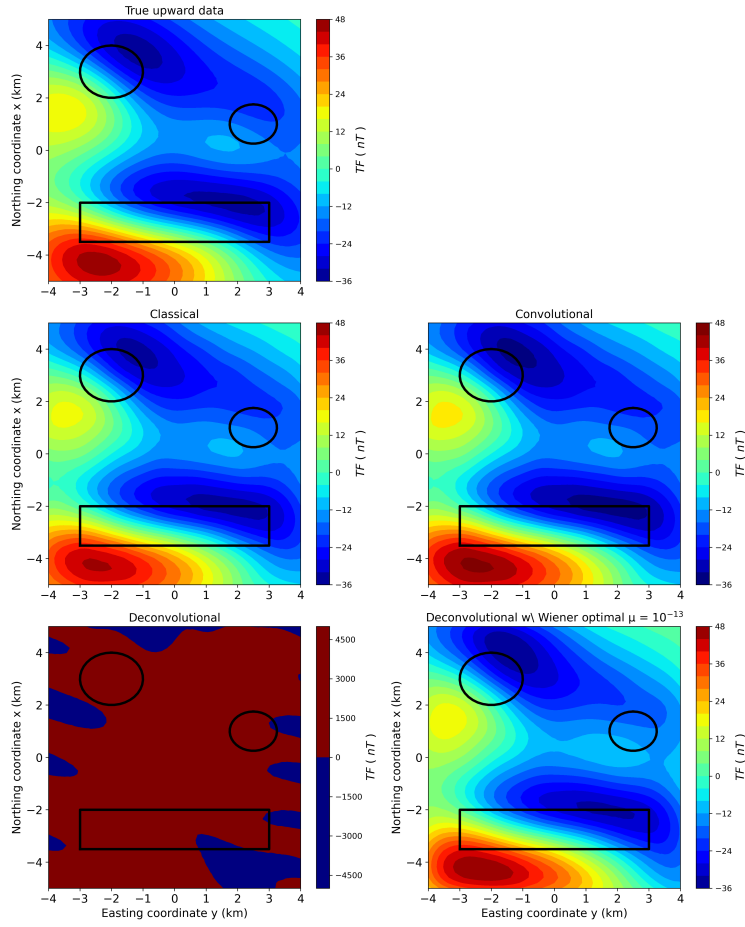


**Figure 9.** True noiseless upward magnetic data at  $z_i = -1400$  m height and predicted data for different methods of the equivalent layer with maximum level of noise. Panel (A) is the true upward magnetic data, Panel (B) is the classical method, (C) is the convolutional, (D) is the deconvolutional, (E) is the deconvolutional method using Wiener stabilization with a optimal value for  $\mu = 10^{-13}$ .

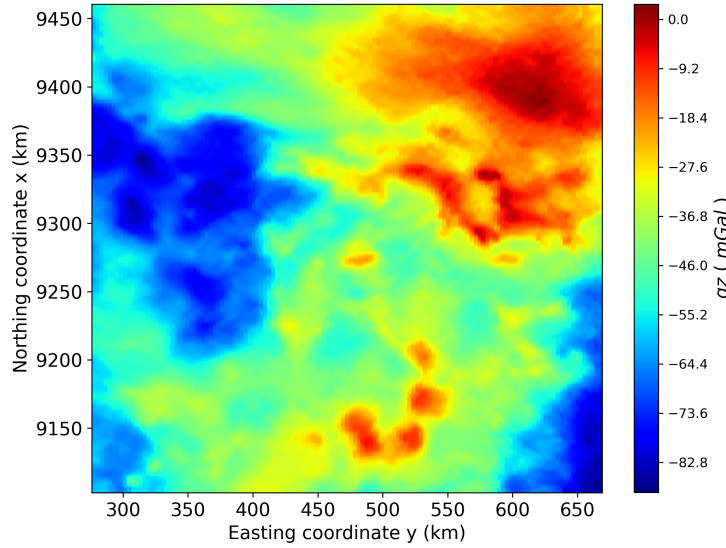


**Figure 10.** Gridded real aerogravimetric data from Carajás, Brazil. A regular grid of  $1,000 \times 500$  is being used, totalizing  $N, M = 500,000$  obsevation points and equivalent sources.

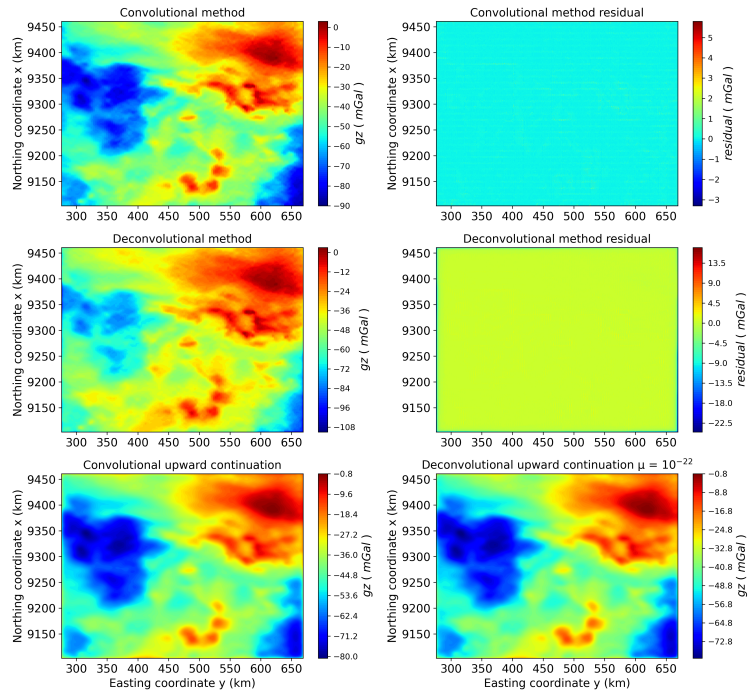


**Figure 11.** Panel (A) shows the Carajás predicted gravimetric data from convolutional equivalent layer method. Panel (B) shows the residual from the convolutional equivalent layer method. Panel (C) shows the predicted data from deconvolutional equivalent layer method. Panel (D) shows the residual from the deconvolutional equivalent layer method. Panel (E) shows the upward continuation at  $z_i = -3500$  m for the convolutional method and Panel (F) shows the upward continuation at  $z_i = -3500$  m for the deconvolutional method.

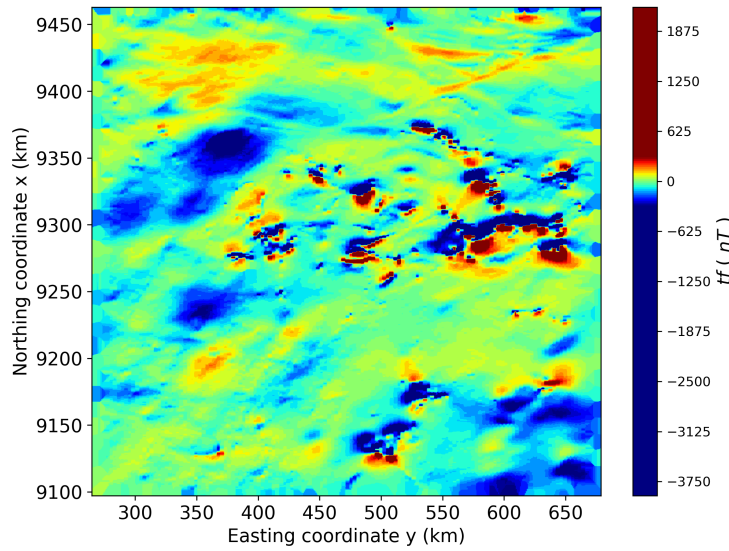


**Figure 12.** Gridded real aeromagnetic data from Carajás, Brazil. A regular grid of  $1,000 \times 500$  is being used, totalizing  $N, M = 500,000$  obsevation points and equivalent sources.

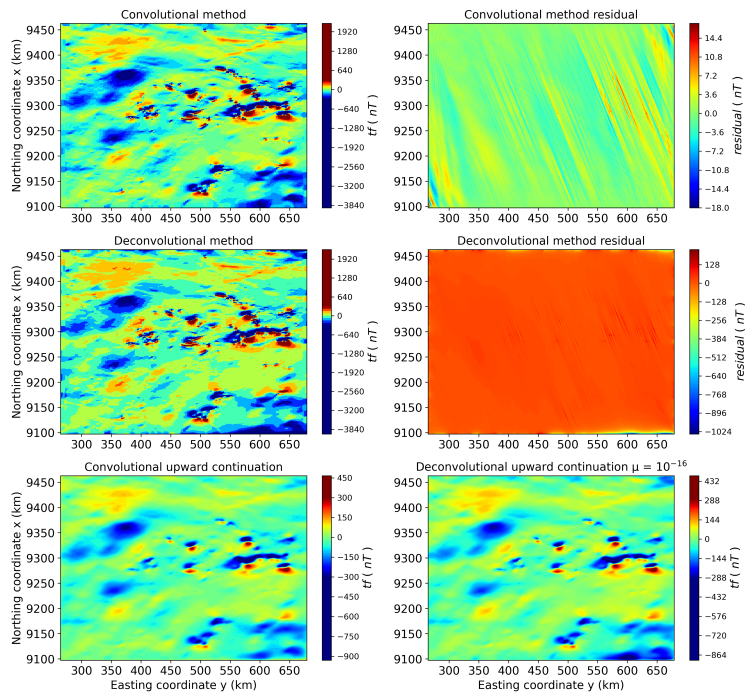


**Figure 13.** Panel (A) shows the Carajás predicted magnetic data from convolutional equivalent layer method. Panel (B) shows the residual from the convolutional equivalent layer method. Panel (C) shows the predicted data from deconvolutional equivalent layer method. Panel (D) shows the residual from the deconvolutional equivalent layer method. Panel (E) shows the upward continuation at  $z_i = -3500$  m for the convolutional method and Panel (F) shows the upward continuation at  $z_i = -3500$  m for the deconvolutional method.